Disordered C-terminal domain drives spatiotemporal confinement of RNAPII to enhance search for chromatin targets

Yick Hin Ling[1], Joseph Ye[1,*], Chuofan Yu[1,*], Chloe Liang[1,*], Giho Park[1,*], Jeffry Corden[2] and Carl Wu[1,2]

[1]Department of Biology, Johns Hopkins University, Baltimore, USA
[2]Department of Molecular Biology and Genetics, Johns Hopkins University School of Medicine, Baltimore, USA
[*]Equal contribution

Abstract

Efficient gene expression demands RNA Polymerase II (RNAPII) to find chromatin targets precisely in space and time. How RNAPII manages this complex diffusive search in a 3D nuclear space remains largely unknown. The disordered carboxy-terminal domain (CTD) of RNAPII, which is essential for recruiting transcription-associated proteins, forms phase-separated droplets *in vitro*, hinting at a potential role in modulating RNAPII dynamics. Here, we use single-molecule tracking and spatiotemporal mapping in living yeast to show that the CTD is responsible for confining RNAPII diffusion within a subnuclear region enriched for active genes, but without apparent phase separation into condensates. Both Mediator and global chromatin organization are required for sustaining RNAPII confinement. Remarkably, truncating the CTD disrupts RNAPII spatial confinement, prolongs target search, diminishes chromatin binding, impairs pre-initiation complex formation, and reduces transcription bursting. This study illuminates the pivotal role of the CTD in driving spatiotemporal confinement of RNAPII for efficient gene expression.

Introduction

The carboxy-terminal domain (CTD) of RPB1 (Rpo21 in yeast), the largest subunit of RNA Polymerase II (RNAPII), is an essential and unique structural feature crucial for transcription regulation in eukaryotes. Defined by its intrinsically disordered structure[1] and consensus heptad repeats (YSPTSPS)[2], the CTD acts as a docking platform for recruiting transcription-associated proteins to interact with RNAPII[3-5]. Notably, the number of the heptad repeats in the CTD correlates with genome size throughout eukaryotes[6-8].

The biochemical properties of intrinsically disordered regions (IDRs), including the CTD, allow liquid-liquid phase separation (LLPS) through weak-multivalent transient interactions[9-11]. This results in the formation of phase-separated transcription condensates comprising RNAPII, the Mediator complex and other transcription-related proteins. These condensates have been proposed to play a critical role in organizing the transcription machinery to facilitate gene regulation[9-14]. By creating a specialized subnuclear environment, LLPS

may help increase the concentration of RNAPII and associated factors for efficient transcription[15,16]. *In vitro*, the ability of the biochemically purified CTD to form phase-separated droplets depends on its length. For example, the human RNAPII CTD, which has 52 heptad repeats, twice as many as its yeast counterpart with 26 repeats, readily forms larger droplets[9,11]. An unresolved question is whether phase-separated RNAPII condensates represent a universally conserved mechanism, or if weak interactions driven by disordered CTDs can guide RNAPII diffusion without transitioning into a condensed phase. Here, we combined live-cell, single-molecule tracking with yeast genetics to elucidate the intricate diffusive mechanisms of RNAPII and the causal dependencies of its target search. Our results show that the diffusing RNAPII is spatially confined, but does not instigate formation of phase-separated condensates on a microscopic scale. The spatial confinement of RNAPII is governed by the full-length CTD, and requires both Mediator and global yeast chromatin organization. Importantly, such confinement allows freely diffusing RNAPII to stochastically oversample subnuclear regions enriched with active genes, establishing a highly efficient target search mechanism to enhance pre-initiation complex (PIC) formation and transcription bursting. Our work demonstrates how RNAPII leverages its search strategy as a rate-limiting step to promote transcription activation, providing insights on the functional significance of the CTD in regulating the spatiotemporal dynamics of RNAPII.

Spatiotemporal mapping of transcription machinery

We performed live-cell single-molecule tracking (SMT) of fluorescently labeled endogenous RNAPII and other transcription proteins fused to HaloTag, and expressed as sole source under native promoter control (Fig. 1b, Extended Data Fig. 1e). Molecule trajectories were categorized into chromatin-bound or freely diffusing states based on diffusivity, geometry and angular orientation using a multi-parameter classification approach (Fig. 1a, Extended Data Fig. 1d and 2, and Supplementary Methods). To extract the spatiotemporal dynamics of the transcription machinery in the small budding yeast nucleus, we developed a mapping method for a strain with GFP markers delineating the plasma membrane, nuclear envelope and the nucleolus (Extended Data Fig. 1a–c and Supplementary Video 1). The method involves selection of G1 phase cells with minimal nuclear drift (Extended Data Fig. 1g and 3a), normalization of trajectory positions based on nuclear landmarks, and superposition of single-molecule localizations from multiple (>10) cell nuclei (Fig. 1a). This maps the spatial distribution of chromatin-bound and freely diffusing proteins over an integrated timeframe, and is grounded in the physical constraints imposed on the centromeres and telomeres of yeast interphase chromatin[17-20] (Extended Data Fig. 1b). A similar mapping approach was previously described for the spatial localization of a single gene locus in

yeast[21]. We interpret the spatiotemporal map density as the probability density of protein localization over time (rather than protein clustering).

We validated the method by mapping the trajectories of free HaloTag, chromatin-bound centromeric Cse4 and telomeric Sir4 trajectories to the expected subnuclear regions (Extended Data Fig. 3e–g). We next examined essential transcription proteins RNAPII, RNAPI, RNAPIII, TFIID and SAGA, showing their free and bound diffusion coefficient distribution and fractions (Fig. 1b). Unlike the semi-homogenous H2B density map (Fig. 1c; bottom), the bound transcription protein maps (Fig. 1c) are uniquely distinct, and spatially mimic the corresponding functional gene classes located by 3D genome simulation[22] (Fig. 1d). Notably, chromatin-bound TFIID and SAGA exhibit distinct spatial territories in the spatiotemporal maps (Fig. 1c), mirroring the TATA-less and TATA-containing genes[23] respectively in the genome simulations (Fig. 1d). This suggests potential co-regulation within these gene classes due to spatial proximity[24]. Further investigation is needed to fully understand the implications of this organization.

CTD governs chromatin binding and spatial confinement of free RNAPII

We compared the spatiotemporal distribution and diffusivity of RNAPII with RNAPI and RNAPIII, given their structural similarities. Freely diffusing RNAPII shows a higher degree of nucleolar exclusion (Extended Data Fig. 4a–c), and diffuses more slowly than expected from its molecular weight (Extended Data Fig. 4d). We hypothesized that the distinct spatiotemporal dynamics of freely diffusing RNAPII might be attributed to its large hydrodynamic radius due to the presence of the disordered CTD[25,26], a feature absent in RNAPI and RNAPIII (Fig. 2a and Extended Data Fig. 4e–j). Notably, we observed that increasing CTD length led to increased nucleolar exclusion and decreased diffusion coefficient of free RNAPII (D_{free}), with the opposite observed for CTD truncations (Fig. 2b,c and Extended Data Fig. 5a). This indicates that CTD length modulates the diffusivity and distribution of free RNAPII between nucleolus and nucleoplasm. Specifically, a large hydrodynamic radius, conferred by a long and highly disordered CTD, may limit diffusion of RNAPII into the nucleolus via size exclusion, thereby increasing its effective concentration in the nucleoplasm.

Next, we explored the impact of CTD length on the chromatin-bound population of RNAPII. Progressive truncation of the CTD from 26 repeats to 10, 9, 8, and 0 repeats notably reduces the bound fraction of RNAPII, while CTD mutants expanded to 52, 78, and 104 repeats show a trend towards increased chromatin-binding (Fig. 2d,e). This trend remains consistent after normalizing nuclear RPB1^{Rpo21} fluorescence intensity to the expression level across mutants[8] (Extended Data Fig. 5c,d). Subsequent investigations in this study primarily focus on CTD truncations due to their pronounced effects. The spatiotemporal maps of bound RNAPII show a global reduction of RNAPII

binding for truncated CTD strains (Fig. 2f; top). Importantly, the map of free RNAPII shows spatial confinement in a subnuclear region enriched for the bound fraction (Fig. 2f), an area also abundant in highly expressed genes (Fig. 1d and Extended Data Fig. 3d). This confinement is disrupted in the CTD9 mutant, and further reduced in the CTD0 strain (Fig. 2f; bottom). Hence, the CTD has a critical role in the spatiotemporal dynamics for both bound and free RNAPII.

RNAPII confinement characterized by anisotropic diffusion depends on CTD, Mediator and 3D chromatin organization

We quantified the spatiotemporal confinement of freely diffusing RNAPII by analyzing its angle distribution within trajectories and anisotropy (Fig. 3a,b and Supplementary Video 3). Anisotropy was measured by ratio of extreme backward to forward angles ($f_{180/0}$) of free trajectories in the nucleoplasm, with confined trajectories showing backward bias[27] (Fig. 3b; top). We observed a substantial backward bias in WT RNAPII (CTD26), which is largely absent for CTD9 and CTD0 mutants, and free HaloTag (Fig. 3a,b). On the other hand, CTDs expanded to 52, 78, and 104 repeats show increasing anisotropy (Extended Data Fig. 5c). A $f_{180/0}$ peak around 150 nm (Fig. 3b) suggests RNAPII confinement within potential domains, as reported for CTCF in mammalian cells, in which anisotropic diffusion through transient trapping in zones has been proposed as an explanatory model[27]. Given that yeast interphase chromosomes are physically tethered to the nuclear envelope via telomeres, we disrupted global chromatin organization by inducing telomere detachment through deletion of *esc1* and *yku70*[28] (Fig. 3c,d and Supplementary Video 4). This resulted in a slight reduction of RNAPII binding (Fig. 3e). Notably, telomere detachment abolishes the $f_{180/0}$ peak at 150 nm in RNAPII, but maintains elevated $f_{180/0}$ across length scales as compared to the $f_{180/0}$ of CTD truncation mutants (Fig. 3f,g). This suggests that global chromatin organization might be required for establishing transient trapping zones or domains that contribute to RNAPII confinement kinetics.

Given the reported weak interactions between mammalian Mediator IDRs and RNAPII CTD *in vitro*[11], we investigated the role of Mediator in RNAPII diffusion. We observed a significant reduction of RNAPII binding when Mediator is degraded using an auxin-inducible degron strain (MED14^{Rgr1} AID) (Fig. 3h,i). Importantly, there is a large reduction of backward bias as shown in the angle distribution plots and anisotropy for free RNAPII (Fig. 3j,k). Furthermore, spatiotemporal mapping indicates a considerable decrease in free RNAPII spatial confinement following Mediator degron (Extended Data Fig. 7e). To further explore the spatiotemporal correlation between Mediator and RNAPII, we found that the map of bound Mediator partially overlaps with the map of confined

RNAPII (Extended Data Fig. 7c,d). Taken together, we conclude that Mediator is functionally linked to RNAPII diffusion confinement.

No substantial RNAPII clustering observed in yeast nucleoplasm

The confined diffusion of RNAPII raises the question of phase separation in condensates. We did not observe fluorescent RNAPII puncta under wide-field microscopy in RPB1^{Rpo21}-HaloTag fusions harboring WT or CTD mutants with reduced or expanded repeats (Fig. 4a). To investigate the possibility of nanoscale puncta, we performed fixed-cell stochastic optical reconstruction microscopy (STORM) on RPB1^{Rpo21}-HaloTag co-stained with JF552 and JFX650. We imaged two color channels simultaneously and performed pairwise cross-correlation C(r) analysis to account for clustering artifacts due to fluorophore blinking[29] (Fig. 4b). The results show no significant clustering of RNAPII-CTD26, with C(r) value close to 1, suggesting a spatial distribution close to random. This low C(r) value is comparable to that of H2B and RNAPII-CTD9 (Fig. 4c).

Given the possibility that transient clusters could be missed by imaging of fixed cells, we replicated the co-staining experiment using live yeast. We analyzed the data using multiple short time windows for potential time-correlated detections[13], and performed Monte Carlo simulations to account for high C(r) values resulting from the limited number of detections within brief observation windows. Nonetheless, we found no strong statistical evidence for transient RNAPII clustering within specific time windows (Fig. 4d; top). Notably, pairwise correlation g(r) analysis performed using only JF552 indicated strong clustering due to repetitive fluorophore blinking or overcounting of fluorophores with extended lifetimes (Fig. 4d; bottom), which underscores the importance of two-color staining for reliable cluster assessment[29]. Thus, the observed high density of free RNAPII over time in our spatiotemporal map (Fig. 2f; bottom) results from transient confinement, rather than stable clustering or phase separation into condensates. This implies that despite the spatial confinement of RNAPII in subnuclear regions, its overall distribution at any given time remains broadly homogeneous.

CTD length is critical for efficient RNAPII target search kinetics

To further investigate the role of the CTD in controlling the chromatin binding kinetics of RNAPII, we measured residence time of individual RNAPII binding events using the 'slow-tracking' SMT mode that minimizes photobleaching with low laser power (Fig. 5b, Extended Data Fig. 8c,d and Supplementary Video 5). Halo-H2B cells were imaged as a spike-in control to correct for photobleaching and chromatin movements out of the focal plane (Fig. 5a and Extended Data Fig. 8f). We observed an average stable residence time of ~20 s for WT RNAPII, which encompasses nonproductive and productive pre-initiation, initiation, elongation, and termination.

For RNAPII-CTD9, this average value is reduced substantially to ~10 s, and the stably bound fraction decreases from ~16% to ~3% (Fig. 5c–e). The short residence time of RNAPII-CTD9 is likely a consequence of the failure of RNAPII to progress beyond the PIC stage at promoters (see below) (Fig. 5j). Similarly, when Mediator is degraded by auxin-inducible degron (MED14^{Rgr1} AID), the RNAPII stably bound fraction is decreased, and the residence time even further reduced to ~5 s (Fig. 5g–i), consistent with previous ChIP results showing depletion of RNAPII occupancy across nearly all genes under similar degron conditions[30].

We estimated the target search time of RNAPII, i.e. the average search duration for an RNAPII molecule between two stable binding events including intervening 3D diffusion and multiple transient chromatin associations, to be ~120 s (Fig. 5f). Although there is no significant change of target search time for the telomere attachment mutant *esc1*Δ *yku70*Δ, we found that the CTD9 mutant indeed shows prolonged RNAPII target search, increasing from the WT value of ~120 s to ~350 s (Fig. 5f). This observation is consistent with the marked reduction in $f_{180/0}$ (Fig. 3b), and in spatial confinement of CTD9 and CTD0 mutants (Fig. 2f; bottom), suggesting that spatiotemporal confinement of RNAPII facilitates its search for and association with promoter chromatin.

CTD regulates spatiotemporal dynamics of PIC components and *HSP82* transcription bursting

Next, we examined the effects of CTD truncation on the dynamics of PIC components. Strikingly, in the CTD9 mutant, the bound fraction of Mediator, TFIIA, TFIIB, TFIIE, TFIIF, and TFIIK is substantially decreased, while SAGA, TFIID and TFIIH show limited changes (Fig. 6a,b). The small change of TFIIH binding was unexpected, given its established function in transcription initiation following PIC formation. This result could be due to the role of TFIIH in DNA repair[31,32], or to unknown complexities of TFIIH in the transcription pathway requiring further investigation. Overall, truncation of the CTD impairs PIC formation in live cells, providing unanticipated insights into the importance of CTD contributions to PIC formation or stability. We additionally detected a substantial decrease in the anisotropy ($f_{180/0}$) for freely diffusing TFIIA, TFIIB, TFIIE, and TFIIF in the CTD9 mutant (Fig. 6c). This could be due to disruption of potential weak interactions between the CTD and these general transcription factors (GTFs). Notably, TFIIA, TFIIE and TFIIF are highly disordered proteins (Fig. 6d-f).

We next examined transcription changes in the CTD9 mutant, focusing on heat shock genes because of the temperature-sensitive CTD9 mutant phenotype[33]. Hsf1, the master transcriptional regulator of the heat shock genes[34], constitutively associates with heat shock elements (HSEs) at the promoter[35-38] under both non-heat shock (NHS) and heat shock (HS) conditions (Fig. 7f). The spatiotemporal map reveals a high density of bound Hsf1 near the nuclear envelope, similar to highly expressed Hsf1 gene targets in the 3D genome simulation map (Fig. 7a,b).

Hsf1 is highly dynamic, with over ~85% of molecules which are freely diffusing (Fig. 7c and Extended Data Fig. 9a). Heat shock induction increases Hsf1 binding from ~10% to ~20% (stable binding from ~2% to ~5%) during acute response (0–20 min at 39°C) (Fig. 7c,d), maintaining a ~5 s residence time for NHS and acute HS (Fig. 7e and Extended Data Fig. 9b). Prolonged HS (20–40 min at 39°C) slightly reduces Hsf1 binding to ~15% (~3% stable binding) (Fig. 7c,d and Extended Data Fig. 9a), with a decrease of residence time to ~2.5 s (Fig. 7e and Extended Data Fig. 9b). In CTD9 mutant, Hsf1 binding and residence time during the acute heat shock response remains largely unchanged (Fig. 7c–e and Extended Data Fig. 9a,b), suggesting that CTD truncation has a minimal impact on the observed binding dynamics of the upstream transcription factor Hsf1.

To address the functional consequences of CTD truncation, we focused on *HSP82*, a gene governed by Hsf1 that is expressed constitutively and is highly inducible under heat shock. Previous research has emphasized the importance of CTD length in the transcription bursting of *GAL* genes[8], which are expressed only under inducible conditions. It remains unclear whether the CTD controls the burst kinetics of constitutively expressed genes. We examined transcription bursting of *HSP82* by imaging the binding of fluorescently-tagged PP7 coat protein (PP7CPx2-mScarlet-Ix3) to a 24xPP7 sequence inserted into the 5' UTR of the nascent *HSP82* mRNA (Fig. 7f,g and Supplementary Video 6). Strong fluorescent foci of PP7CPx2-mScarlet-Ix3 representing *HSP82* transcription sites (TSs), frequently appear near the nuclear envelope (Fig. 7h-j), consistent with the spatiotemporal map of bound Hsf1 (Fig. 7a,b). Under nonshock conditions, CTD9 shows a lower percentage of cells with *HSP82* TS fluorescence (~78%) compared to WT (~96%). However, upon heat shock, TS fluorescence appears almost instantaneously in nearly all cells for both WT and CTD9 mutant strains (Fig. 7k,l). We calculated the corresponding transcription ON and OFF times after binary conversion of *HSP82* TS signals (Fig. 7k). For WT CTD26, acute heat shock increases *HSP82* ON from ~3 min to ~4.5 min, while decreasing OFF from ~7 min to ~2 min. For prolonged heat shock, the ON time is similar to nonshock conditions, while OFF time is reduced to ~3 min (Fig. 7m,n, and Extended Data Fig. 9c,d), anticipating attenuation of the heat shock response. Notably, in all conditions, the CTD9 mutant consistently reduces ON time (lower burst duration) and increases OFF time (lower burst frequency) of *HSP82* transcription (Fig. 7m,n and Extended Data Fig. 9c,d), indicating that full CTD length is required for proper burst kinetics under both constitutive and heat shock conditions. This finding offers a molecular explanation for the temperature-sensitive phenotype observed for the CTD9 mutant[33]. Importantly, the reduction in both duration and frequency of transcription bursting indicates that the diffusion confinement of RNAPII in the nucleoplasm could regulate the rate-limiting search for chromatin targets in the transcription cycle to sustain a transcription burst. The number of intrinsically disordered CTD repeats is central to this spatiotemporal

confinement.

Discussion

We have extended single-molecule tracking (SMT) to develop global spatiotemporal maps of transcription protein dynamics in living yeast (Fig. 1). This approach reveals that the disordered CTD of RNAPII, with a WT length of 26 heptad repeats, directs the confinement of RNAPII within a subnuclear region enriched for active genes (Fig. 2). Characterization of anisotropic diffusion of RNAPII shows its dependence on the full-length CTD, chromatin organization and the presence of Mediator (Fig. 3). RNAPII exhibits transient confinement without phase separation into condensate (Fig. 4). Importantly, the number of CTD repeats critically influences RNAPII search kinetics (Fig. 5) and PIC formation (Fig. 6). Functionally, CTD truncation disrupts transcription burst kinetics of *HSP82* (Fig. 7).

Our observations in yeast demonstrate that RNAPII show no substantial clustering, challenging the generality of LLPS for the spatial organization of RNAPII. For eukaryotes with larger nuclei and genome complexity, additional spatial control and dynamic phase-separated compartments might be necessary for long range promoter-enhancer interaction, although this is a topic of ongoing study[39,40]. In yeast, however, the strong physical constraints and tethering imposed on chromatin[17-20] could create genomic domains enriched for active genes (Fig. 1c,d), facilitating RNAPII confinement without the need for phase separation into condensates (Fig. 3 and 4). Furthermore, a biochemical environment in the yeast nucleoplasm that is inhibitory to phase separation cannot be excluded. For example, LLPS-prone FUS protein forms foci in the yeast cytoplasm (by incorporating into stress granules and P-bodies), but not in the yeast nucleus[41].

What might be the molecular basis of this confinement of RNAPII? *In vitro* evidence of weak interactions between CTD and Mediator IDRs[11] suggests a mechanism by heterotypic IDR-IDR interactions. Consistent with this, degradation of the Mediator largely reduces RNAPII confinement (Fig. 3j,k and Extended Data Fig. 7e), and the maps of bound Mediator and confined RNAPII do partially overlap (Extended Data Fig. 7c,d). In addition to the heterotypic weak interactions, homotypic interactions between the CTD have been identified *in vitro*[9,10]. Imaging of the CTD fused to GFP shows evidence of enrichment at transcriptionally active loci of *Drosophila* polytene chromosomes *in vivo*[42], raising the question whether the CTD alone is sufficient to drive its own spatiotemporal confinement in living yeast. Our supplementary observations show that HaloTag alone and Halo-CTD fusions harboring 26, 52, 78, and 104 heptad repeats expressed under control of the natural *RPO21* promoter exhibit minimal chromatin binding (Extended Data Fig. 10a), show no puncta (Extended Data Fig. 10b), and D_{free} values align with the Stokes-Einstein equation, indicating uniform nucleoplasmic viscosity (~30 cP) without phase

separation (Extended Data Fig. 10d-g). Furthermore, Halo-CTD mutants do not exhibit high $f_{180/0}$ values, indicating that diffusion is relatively isotropic or unconfined (Extended Data Fig. 10h). Evidently, at physiological expression levels, the CTD alone does not induce the same degree of diffusion confinement as observed for the RNAPII complex. Thus, the CTD is necessary, but not sufficient for the spatiotemporal confinement of RNAPII, and additional factors or domains within the RNAPII complex might come into play (e.g. TFIIF, which is predominantly recruited in association with RNAPII and has high intrinsic disorder (Fig. 6d-f)).

Our data suggest that diffusion confinement of RNAPII dependent on CTD repeats facilitates the rate-limiting search for chromatin targets early in the transcription cycle (Fig. 8). We propose that the heterotypic IDR-IDR interactions among Mediator, CTD and GTFs increase specific association rates for formation of a complete PIC. These weak-multivalent interactions govern spatiotemporal confinement of protein factors at physiological expression levels evidently below the threshold for phase separation into condensate. A dynamic, fuzzy 'pre-PIC cloud', characterized by transient weak interactions between components, may form near promoters until all essential components including RNAPII become engaged at promoter DNAs for repeated rounds of pre-initiation, initiation, and elongation to generate a transcription burst. Our study emphasizes the crucial role of the CTD in driving RNAPII target search and shaping the spatiotemporal dynamics of PIC assembly, highlighting its multifaceted functions in the pathway to gene expression.

Acknowledgments

We thank Scarlet Cho and Gan Ling for assistance in image processing; Luke Lavis for providing Janelia Fluor dyes; Kelly Xie for IUPRED3 data mining; Xiaona Tang and Sheng Liu for computational assistance; Nathan Jones, Vincent Schoonderwoert and Ciprian Almonte for microscopy technical support; Karen Yuen and Gaku Mizuguchi for plasmids and yeast strains; Charmaine Wong, Jee Min Kim, Ibrahim Cissé and Anders Hansen for helpful discussions; and members of the Wu laboratory for comments. This study was supported by National Institute of Health grant GM132290-01 (C.W.) and the Croucher Foundation (Y.H.L.).

Author information

These authors contributed equally: Joseph Ye, Chuofan Yu, Chloe Liang, Giho Park

Authors and Affiliations

Department of Biology, Johns Hopkins University, Baltimore, USA

Yick Hin Ling, Joseph Ye, Chuofan Yu, Chloe Liang, Giho Park, Carl Wu

Department of Molecular Biology and Genetics, Johns Hopkins University School of Medicine, Baltimore, USA

Jeffry Corden, Carl Wu

Contributions

Y.H.L., J.C., and C.W. designed the experiments. Y.H.L. performed the experiments and analyzed the data. J.Y. performed SMT on Hsf1-Halo in the wildtype background. G.P. contributed to the initial trial of spatiotemporal mapping. J.Y., C.Y., and C.L. assisted in experiments. Y.H.L., J.C., and C.W. wrote the manuscript.

Methods

Extended Data Figures

Extended Data Figures 1-10

Supplementary information

Supplementary Methods, Supplementary Tables 1,2, Supplementary Figures 1,2 and references.

Supplementary Videos 1-6

References

1. Cramer, P., Bushnell, D. A. & Kornberg, R. D. Structural basis of transcription: RNA polymerase II at 2.8 angstrom resolution. Science 292, 1863-1876, doi:10.1126/science.1059493 (2001).
2. Corden, J. L. RNA polymerase II C-terminal domain: Tethering transcription to transcript and template. Chem Rev 113, 8423-8455, doi:10.1021/cr400158h (2013).
3. Eick, D. & Geyer, M. The RNA polymerase II carboxy-terminal domain (CTD) code. Chem Rev 113, 8456-8490, doi:10.1021/cr400071f (2013).
4. Harlen, K. M. & Churchman, L. S. The code and beyond: transcription regulation by the RNA polymerase II carboxy-terminal domain. Nat Rev Mol Cell Biol 18, 263-273, doi:10.1038/nrm.2017.10 (2017).
5. Buratowski, S. Progression through the RNA polymerase II CTD cycle. Mol Cell 36, 541-546, doi:10.1016/j.molcel.2009.10.019 (2009).
6. Chapman, R. D., Heidemann, M., Hintermair, C. & Eick, D. Molecular evolution of the RNA polymerase II CTD. Trends Genet 24, 289-296, doi:10.1016/j.tig.2008.03.010 (2008).
7. Yang, C. & Stiller, J. W. Evolutionary diversity and taxon-specific modifications of the RNA polymerase II C-terminal domain. Proc Natl Acad Sci U S A 111, 5920-5925, doi:10.1073/pnas.1323616111 (2014).
8. Quintero-Cadena, P., Lenstra, T. L. & Sternberg, P. W. RNA Pol II Length and Disorder Enable Cooperative Scaling of Transcriptional Bursting. Mol Cell 79, 207-220 e208, doi:10.1016/j.molcel.2020.05.030 (2020).
9. Boehning, M. et al. RNA polymerase II clustering through carboxy-terminal domain phase separation. Nat Struct Mol Biol 25, 833-840, doi:10.1038/s41594-018-0112-y (2018).
10. Lu, H. et al. Phase-separation mechanism for C-terminal hyperphosphorylation of RNA polymerase II. Nature 558, 318-323, doi:10.1038/s41586-018-0174-3 (2018).
11. Guo, Y. E. et al. Pol II phosphorylation regulates a switch between transcriptional and splicing condensates. Nature 572, 543-548, doi:10.1038/s41586-019-1464-0 (2019).
12. Cho, W. K. et al. RNA Polymerase II cluster dynamics predict mRNA output in living cells. Elife 5, doi:10.7554/eLife.13617 (2016).
13. Cisse, II et al. Real-time dynamics of RNA polymerase II clustering in live human cells. Science 341, 664-667, doi:10.1126/science.1239053 (2013).
14. Cho, W. K. et al. Mediator and RNA polymerase II clusters associate in transcription-dependent condensates. Science 361, 412-415, doi:10.1126/science.aar4199 (2018).
15. Boija, A. et al. Transcription Factors Activate Genes through the Phase-Separation Capacity of Their Activation Domains. Cell 175, 1842-1855 e1816, doi:10.1016/j.cell.2018.10.042 (2018).
16. Wei, M. T. et al. Nucleated transcriptional condensates amplify gene expression. Nat Cell Biol 22, 1187-1196, doi:10.1038/s41556-020-00578-6 (2020).
17. Tjong, H., Gong, K., Chen, L. & Alber, F. Physical tethering and volume exclusion determine higher-order genome organization in budding yeast. Genome Res 22, 1295-1305, doi:10.1101/gr.129437.111 (2012).
18. Gasser, S. M., Hediger, F., Taddei, A., Neumann, F. R. & Gartenberg, M. R. The function of telomere clustering in yeast: the circe effect. Cold Spring Harb Symp Quant Biol 69, 327-337, doi:10.1101/sqb.2004.69.327 (2004).
19. Rosa, A. & Everaers, R. Structure and dynamics of interphase chromosomes. PLoS Comput Biol 4, e1000153, doi:10.1371/journal.pcbi.1000153 (2008).

20. Zimmer, C. & Fabre, E. Principles of chromosomal organization: lessons from yeast. J Cell Biol 192, 723-733, doi:10.1083/jcb.201010058 (2011).
21. Berger, A. B. et al. High-resolution statistical mapping reveals gene territories in live yeast. Nat Methods 5, 1031-1037, doi:10.1038/nmeth.1266 (2008).
22. Duan, Z. et al. A three-dimensional model of the yeast genome. Nature 465, 363-367, doi:10.1038/nature08973 (2010).
23. Huisinga, K. L. & Pugh, B. F. A genome-wide housekeeping role for TFIID and a highly regulated stress-related role for SAGA in Saccharomyces cerevisiae. Mol Cell 13, 573-585, doi:10.1016/s1097-2765(04)00087-5 (2004).
24. Gong, K., Tjong, H., Zhou, X. J. & Alber, F. Comparative 3D genome structure analysis of the fission and the budding yeast. PLoS One 10, e0119672, doi:10.1371/journal.pone.0119672 (2015).
25. Erickson, H. P. Size and shape of protein molecules at the nanometer level determined by sedimentation, gel filtration, and electron microscopy. Biol Proced Online 11, 32-51, doi:10.1007/s12575-009-9008-x (2009).
26. Portz, B. et al. Structural heterogeneity in the intrinsically disordered RNA polymerase II C-terminal domain. Nat Commun 8, 15231, doi:10.1038/ncomms15231 (2017).
27. Hansen, A. S., Amitai, A., Cattoglio, C., Tjian, R. & Darzacq, X. Guided nuclear exploration increases CTCF target search efficiency. Nat Chem Biol 16, 257-266, doi:10.1038/s41589-019-0422-3 (2020).
28. Gartenberg, M. R., Neumann, F. R., Laroche, T., Blaszczyk, M. & Gasser, S. M. Sir-mediated repression can occur independently of chromosomal and subnuclear contexts. Cell 119, 955-967, doi:10.1016/j.cell.2004.11.008 (2004).
29. Hansen, A. S., Pustova, I., Cattoglio, C., Tjian, R. & Darzacq, X. CTCF and cohesin regulate chromatin loop stability with distinct dynamics. Elife 6, doi:10.7554/eLife.25776 (2017).
30. Warfield, L. et al. Transcription of Nearly All Yeast RNA Polymerase II-Transcribed Genes Is Dependent on Transcription Factor TFIID. Mol Cell 68, 118-129 e115, doi:10.1016/j.molcel.2017.08.014 (2017).
31. Schaeffer, L. et al. DNA repair helicase: a component of BTF2 (TFIIH) basic transcription factor. Science 260, 58-63, doi:10.1126/science.8465201 (1993).
32. Feaver, W. J. et al. Dual roles of a multiprotein complex from S. cerevisiae in transcription and DNA repair. Cell 75, 1379-1387, doi:10.1016/0092-8674(93)90624-y (1993).
33. West, M. L. & Corden, J. L. Construction and analysis of yeast RNA polymerase II CTD deletion and substitution mutations. Genetics 140, 1223-1233, doi:10.1093/genetics/140.4.1223 (1995).
34. Wu, C. Heat shock transcription factors: structure and regulation. Annu Rev Cell Dev Biol 11, 441-469, doi:10.1146/annurev.cb.11.110195.002301 (1995).
35. Jakobsen, B. K. & Pelham, H. R. Constitutive binding of yeast heat shock factor to DNA in vivo. Mol Cell Biol 8, 5040-5042, doi:10.1128/mcb.8.11.5040-5042.1988 (1988).
36. Park, H. O. & Craig, E. A. Positive and negative regulation of basal expression of a yeast HSP70 gene. Mol Cell Biol 9, 2025-2033, doi:10.1128/mcb.9.5.2025-2033.1989 (1989).
37. Sorger, P. K. & Pelham, H. R. Purification and characterization of a heat-shock element binding protein from yeast. EMBO J 6, 3035-3041, doi:10.1002/j.1460-2075.1987.tb02609.x (1987).
38. Sorger, P. K. & Pelham, H. R. Yeast heat shock factor is an essential DNA-binding protein that exhibits temperature-dependent phosphorylation. Cell 54, 855-864, doi:10.1016/s0092-8674(88)91219-6 (1988).

39. Hnisz, D., Shrinivas, K., Young, R. A., Chakraborty, A. K. & Sharp, P. A. A Phase Separation Model for Transcriptional Control. Cell 169, 13-23, doi:10.1016/j.cell.2017.02.007 (2017).
40. Lyons, H. et al. Functional partitioning of transcriptional regulators by patterned charge blocks. Cell 186, 327-345 e328, doi:10.1016/j.cell.2022.12.013 (2023).
41. Sun, Z. et al. Molecular determinants and genetic modifiers of aggregation and toxicity for the ALS disease protein FUS/TLS. PLoS Biol 9, e1000614, doi:10.1371/journal.pbio.1000614 (2011).
42. Lu, F., Portz, B. & Gilmour, D. S. The C-Terminal Domain of RNA Polymerase II Is a Multivalent Targeting Sequence that Supports Drosophila Development with Only Consensus Heptads. Mol Cell 73, 1232-1242 e1234, doi:10.1016/j.molcel.2019.01.008 (2019).
43. Lenstra, T. L. & Larson, D. R. Single-Molecule mRNA Detection in Live Yeast. Curr Protoc Mol Biol 113, 14 24 11-14 24 15, doi:10.1002/0471142727.mb1424s113 (2016).
44. Nguyen, V. Q. et al. Spatiotemporal coordination of transcription preinitiation complex assembly in live cells. Mol Cell 81, 3560-3575 e3566, doi:10.1016/j.molcel.2021.07.022 (2021).
45. Zheng, Q. et al. Rational Design of Fluorogenic and Spontaneously Blinking Labels for Super-Resolution Imaging. ACS Cent Sci 5, 1602-1613, doi:10.1021/acscentsci.9b00676 (2019).
46. Grimm, J. B. et al. A general method to improve fluorophores for live-cell and single-molecule microscopy. Nat Methods 12, 244-250, 243 p following 250, doi:10.1038/nmeth.3256 (2015).
47. Vallotton, P. et al. Diatrack particle tracking software: Review of applications and performance evaluation. Traffic 18, 840-852, doi:10.1111/tra.12530 (2017).
48. Persson, F., Linden, M., Unoson, C. & Elf, J. Extracting intracellular diffusive states and transition rates from single-molecule tracking data. Nat Methods 10, 265-269, doi:10.1038/nmeth.2367 (2013).
49. Miura, F. et al. Absolute quantification of the budding yeast transcriptome by means of competitive PCR between genomic and complementary DNAs. BMC Genomics 9, 574, doi:10.1186/1471-2164-9-574 (2008).
50. Luan, J. et al. Distinct properties and functions of CTCF revealed by a rapidly inducible degron system. Cell Rep 34, 108783, doi:10.1016/j.celrep.2021.108783 (2021).
51. Chazeau, A., Katrukha, E. A., Hoogenraad, C. C. & Kapitein, L. C. Studying neuronal microtubule organization and microtubule-associated proteins using single molecule localization microscopy. Methods Cell Biol 131, 127-149, doi:10.1016/bs.mcb.2015.06.017 (2016).
52. Bohrer, C. H. et al. A pairwise distance distribution correction (DDC) algorithm to eliminate blinking-caused artifacts in SMLM. Nat Methods 18, 669-677, doi:10.1038/s41592-021-01154-y (2021).
53. Morawska, M. & Ulrich, H. D. An expanded tool kit for the auxin-inducible degron system in budding yeast. Yeast 30, 341-351, doi:10.1002/yea.2967 (2013).
54. Papagiannakis, A., de Jonge, J. J., Zhang, Z. & Heinemann, M. Quantitative characterization of the auxin-inducible degron: a guide for dynamic protein depletion in single yeast cells. Sci Rep 7, 4704, doi:10.1038/s41598-017-04791-6 (2017).
55. Gesnel, M. C., Del Gatto-Konczak, F. & Breathnach, R. Combined use of MS2 and PP7 coat fusions shows that TIA-1 dominates hnRNP A1 for K-SAM exon splicing control. J Biomed Biotechnol 2009, 104853, doi:10.1155/2009/104853 (2009).
56. Brouwer, I., Kerklingh, E., van Leeuwen, F. & Lenstra, T. L. Dynamic epistasis analysis reveals how chromatin remodeling regulates transcriptional bursting. Nat Struct Mol Biol, doi:10.1038/s41594-023-00981-1 (2023).

57. Li, L., Waymack, R., Gad, M. & Wunderlich, Z. Two promoters integrate multiple enhancer inputs to drive wild-type knirps expression in the Drosophila melanogaster embryo. Genetics 219, doi:10.1093/genetics/iyab154 (2021).
58. Zhang, T. et al. An improved method for whole protein extraction from yeast Saccharomyces cerevisiae. Yeast 28, 795-798, doi:10.1002/yea.1905 (2011).
59. Kovacs, D. et al. HSF1Base: A Comprehensive Database of HSF1 (Heat Shock Factor 1) Target Genes. Int J Mol Sci 20, doi:10.3390/ijms20225815 (2019).
60. Pincus, D. et al. Genetic and epigenetic determinants establish a continuum of Hsf1 occupancy and activity across the yeast genome. Mol Biol Cell 29, 3168-3182, doi:10.1091/mbc.E18-06-0353 (2018).
61. Pontius, B. W. Close encounters: why unstructured, polymeric domains can increase rates of specific macromolecular association. Trends Biochem Sci 18, 181-186, doi:10.1016/0968-0004(93)90111-y (1993).
62. Therizols, P., Duong, T., Dujon, B., Zimmer, C. & Fabre, E. Chromosome arm length and nuclear constraints determine the dynamic relationship of yeast subtelomeres. Proc Natl Acad Sci U S A 107, 2025-2030, doi:10.1073/pnas.0914187107 (2010).
63. Taddei, A. & Gasser, S. M. Structure and function in the budding yeast nucleus. Genetics 192, 107-129, doi:10.1534/genetics.112.140608 (2012).
64. Tsai, K. L. et al. A conserved Mediator-CDK8 kinase module association regulates Mediator-RNA polymerase II interaction. Nat Struct Mol Biol 20, 611-619, doi:10.1038/nsmb.2549 (2013).
65. Knuesel, M. T., Meyer, K. D., Bernecky, C. & Taatjes, D. J. The human CDK8 subcomplex is a molecular switch that controls Mediator coactivator function. Genes Dev 23, 439-451, doi:10.1101/gad.1767009 (2009).
66. Elmlund, H. et al. The cyclin-dependent kinase 8 module sterically blocks Mediator interactions with RNA polymerase II. Proc Natl Acad Sci U S A 103, 15788-15793, doi:10.1073/pnas.0607483103 (2006).
67. Mazza, D., Abernathy, A., Golob, N., Morisaki, T. & McNally, J. G. A benchmark for chromatin binding measurements in live cells. Nucleic Acids Res 40, e119, doi:10.1093/nar/gks701 (2012).

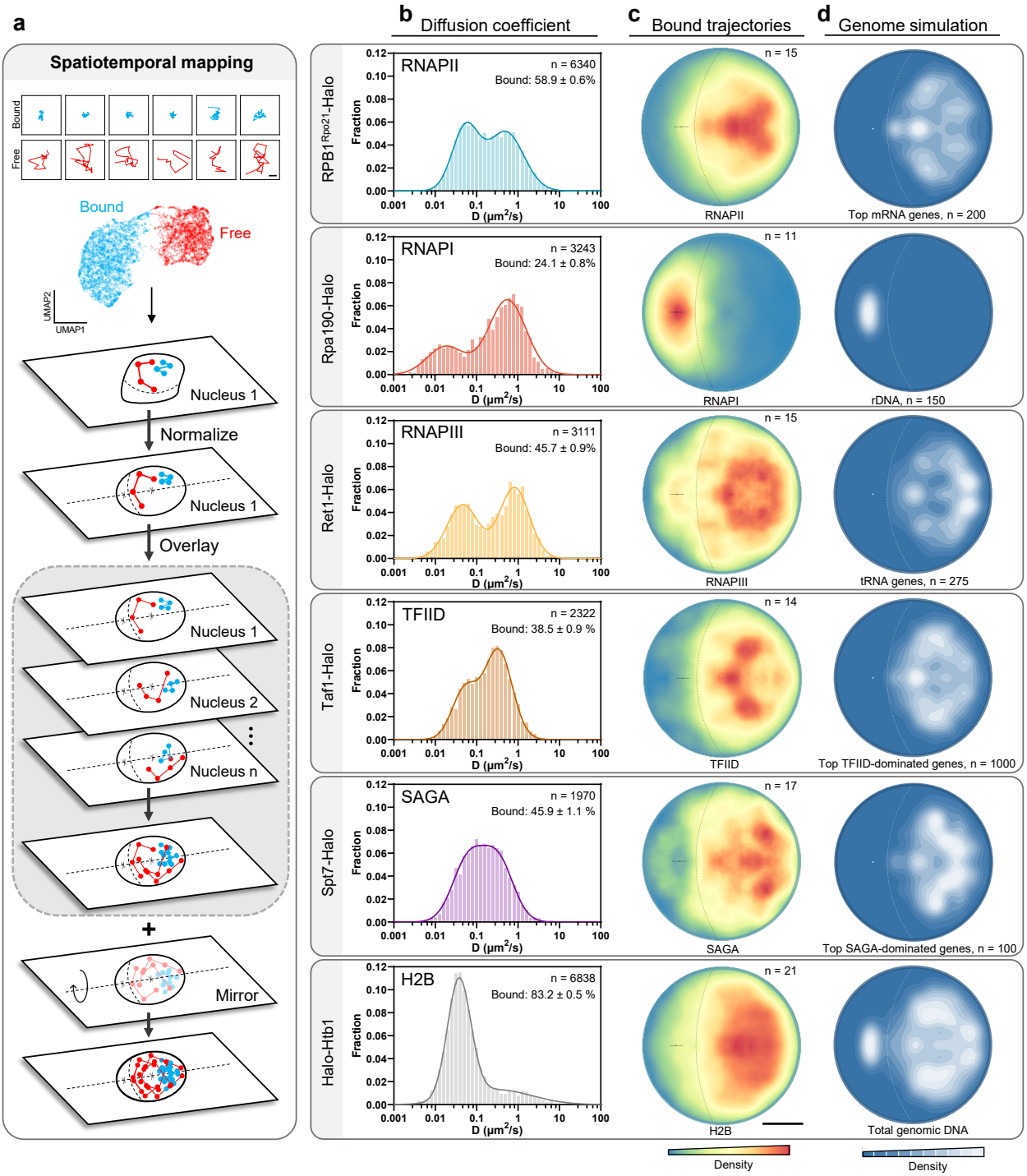

Fig. 1. Spatiotemporal mapping of transcription machinery in living yeast nucleus. a, Spatiotemporal mapping workflow: bound and free trajectories (Scale bar: 0.2 μm) classified by multi-parameter analysis, and single-molecule localization and nuclear radius normalized to a circular model of 1 μm radius. Localizations overlaid from at least 10 nuclei that display minimal drift during image acquisition. Visualization of the spatiotemporal map on a single plane facilitated by mirroring around the central axis[21]. **b**, Diffusion coefficient histograms for RNAPII, RNAPI, RNAPIII, TFIID, SAGA and H2B. Representative HaloTag fusions shown (n: number of trajectories; mean value ± s.d.). **c**, Detection map of chromatin-bound trajectories. Scale bar: 0.5 μm (Error bar: centroid of nucleolus ± s.d.; n: number of nuclei). **d**, Simulation of the spatial distribution of gene classes in yeast nucleus (n: number of genes).

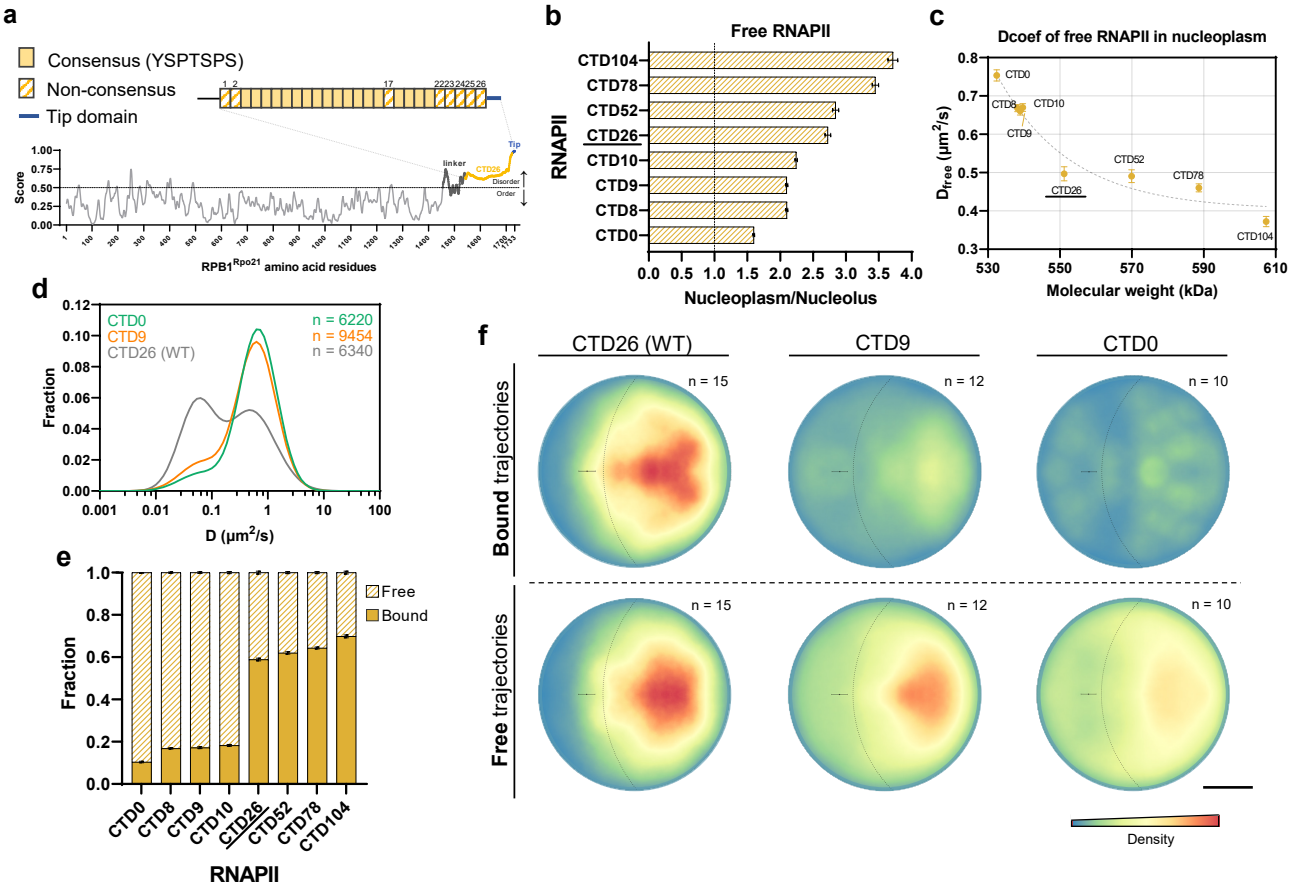

Fig. 2. CTD governs spatiotemporal dynamics of RNAPII. a, Disordered C-terminal domain of RPB1^{Rpo21} consisting of 26 heptad repeats with consensus sequence YSPTSPS. IUPRED3 scores above 0.5 considered disordered. **b**-**f**, Spatiotemporal dynamics of RNAPII and CTD mutants characterized by **b**, freely diffusing population Nucleoplasm/Nucleolus (n = 100 resamplings; mean value ± s.d.), **c**, D_{free} in nucleoplasm (n = 100 resamplings; mean value ± s.d.), **d**, two-component Gaussian fit of diffusion coefficient histograms, **e**, fraction of free and bound (n = 100 resamplings; mean value ± s.d.), and f, spatiotemporal mapping for free and chromatin-bound trajectories. Scale bar: 0.5 μm (Error bar: centroid of nucleolus ± s.d.; n: number of nuclei). Top left panel is reuse of Fig. 1c top panel.

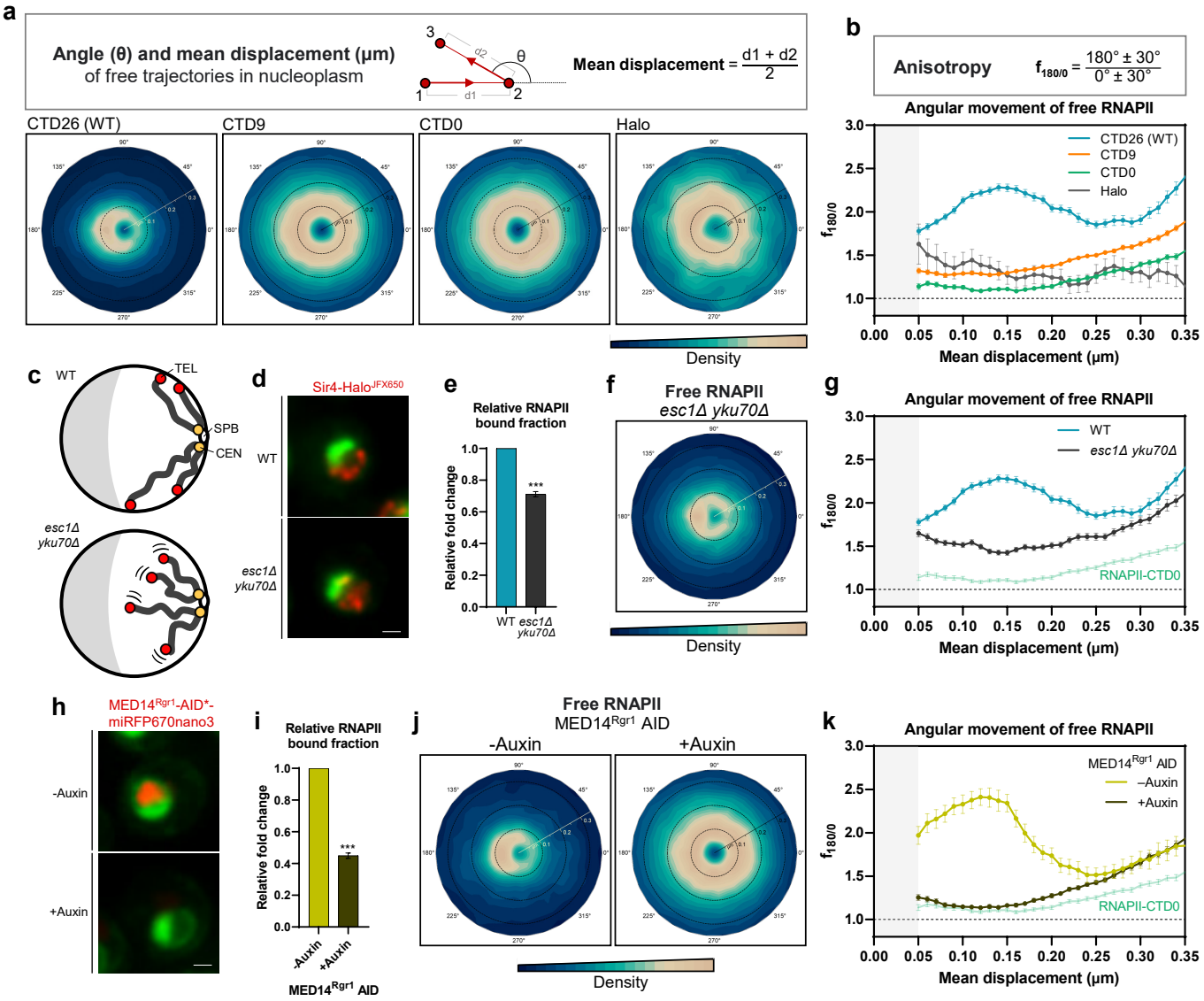

Fig. 3. The interplay of CTD, chromatin organization and Mediator shapes RNAPII anisotropic diffusion. **a**, Angle (angular axis) and mean displacement (radial axis; unit: μm) polar plots of RNAPII, CTD mutants and HaloTag (NLSx2-Halo). **b**, Anisotropic diffusion of freely diffusing of RNAPII, CTD mutants and HaloTag in nucleoplasm measured by $f_{180/0}$ (n = 100 resamplings; mean value ± s.d.). **c**, Impaired telomere (TEL) attachment in *esc1*Δ *yku70*Δ strain. **d**, Fluorescence signal of Sir4-Halo^{JFX650} (red) in WT and *esc1*Δ *yku70*Δ. Nucleolar and ER markers in green. Scale bar: 1.0 μm (Supplementary Video 4). **e**, Relative bound fraction of RNAPII in WT and *esc1*Δ *yku70*Δ strains (n = 100 resamplings; mean value ± s.d.; two-tailed unpaired t-test). **f**, Angle and displacement polar plots of RNAPII in *esc1*Δ *yku70*Δ strain. **g**, $f_{180/0}$ of RNAPII in WT and *esc1*Δ *yku70*Δ strains (n = 100 resamplings; mean value ± s.d.). **h**, Fluorescence signal of MED14^{Rgr1}-AID*-miRFP670nano3 (red) before and after Mediator degradation by auxin treatment. Nucleolar and ER markers in green. Scale bar: 1.0 μm. **i**, Relative bound fraction of RNAPII after Mediator degradation (n = 100 resamplings; mean value ± s.d.; two-tailed unpaired t-test). **j**, Angle and displacement polar plots of RNAPII before and after Mediator degradation. **k**, $f_{180/0}$ of RNAPII before and after Mediator degradation (n = 100 resamplings; mean value ± s.d.).

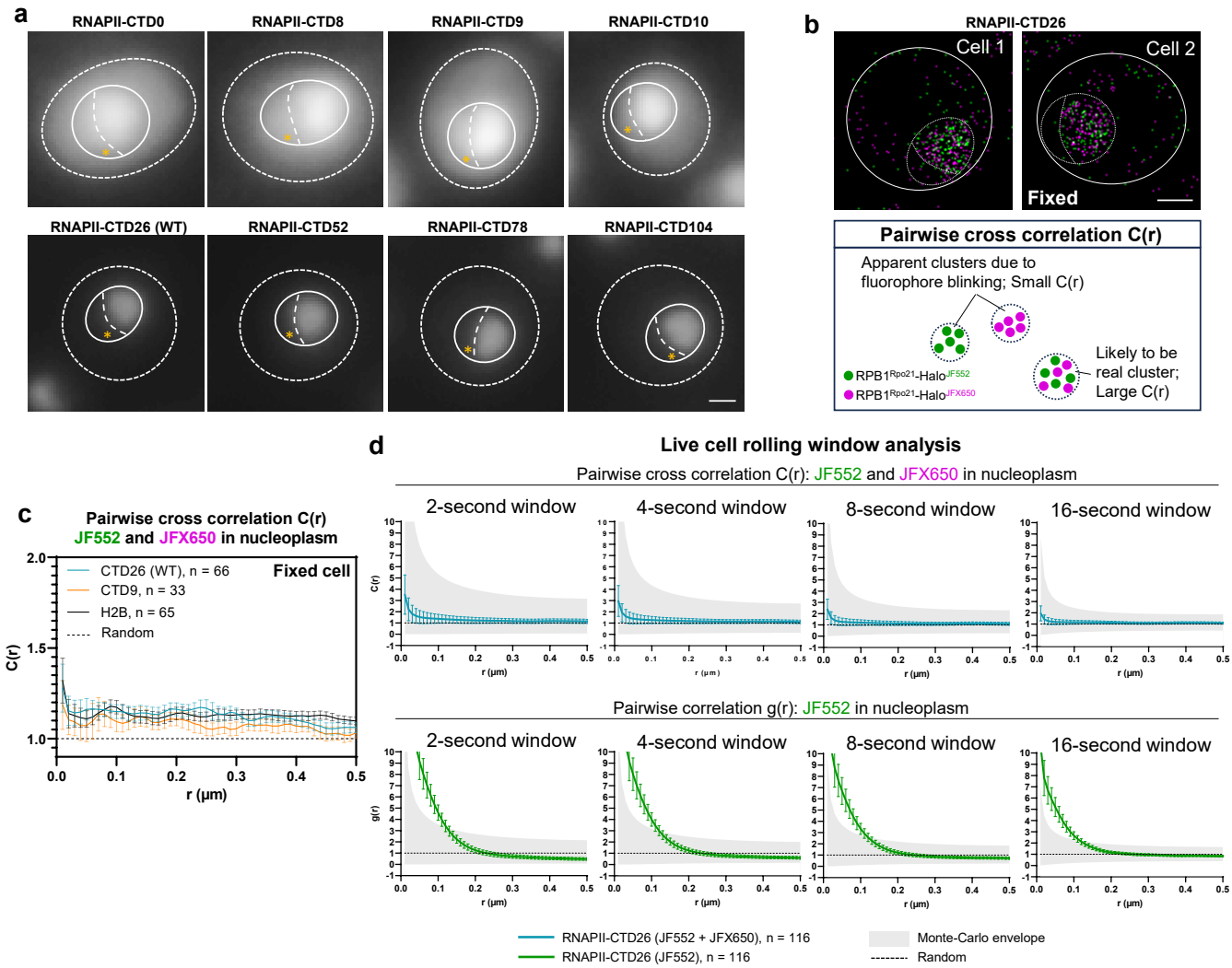

Fig. 4. No substantial RNAPII clustering in yeast nucleoplasm. a, Bulk wide-field staining of RPB1^{Rpo21}-Halo with JFX650 in live cells. Nucleolus indicated by asterisk. Scale bar: 1.0 µm. **b**, RPB1^{Rpo21}-Halo fixed-cell STORM images using JF552 and JFX650. Scale bar: 1.0 µm (top). RNAPII clustering analyzed by pairwise cross-correlation C(r) (bottom). **c**, C(r) of RNAPII-CTD26, RNAPII-CTD9 and H2B in nucleoplasm (n: number of nuclei; mean value ± s.d.). **d**, RPB1^{Rpo21}-Halo rolling window analysis for live cell two-color STORM (n: number of nuclei; mean value ± s.d.).

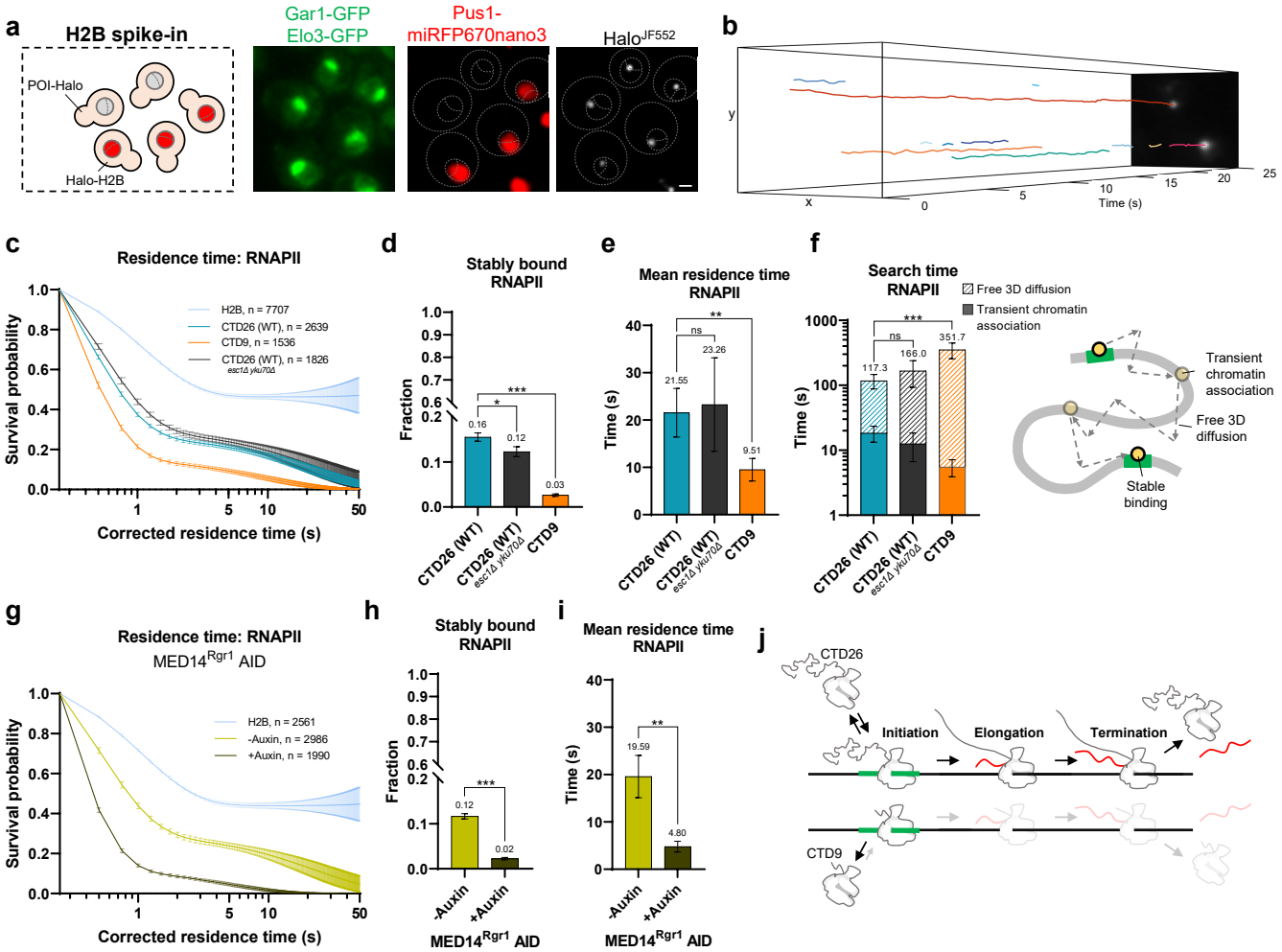

Fig. 5. CTD facilitates RNAPII target-search kinetics. **a**, Halo-H2B cell spike-in for residence time correction with Pus1-miRFP670nano3 nuclear marker. Scale bar: 1.0 µm. **b**, Kymograph of slow tracking trajectories of RNAPII (RPB1^{Rpo21}-Halo) (Supplementary Video 5). **c**, Survival probability of H2B-corrected residence times for bound RNAPII in CTD26 (WT), CTD9 and *esc1*Δ *yku70*Δ strains (n: number of trajectories; mean value ± s.d.). **d**-**f**, **d**, Stably bound fractions, **e**, mean residence times, and **f**, search times (left) of RNAPII in CTD26 (WT), CTD9 and *esc1*Δ *yku70*Δ strains (n = 10,000 resamplings; mean value ± s.d.; two-tailed unpaired t-test). **f**, Simplified mode of target search in the nucleus (right). **g**, Survival probability of H2B-corrected residence times of RNAPII before and after Mediator degradation (MED14^{Rgr1} AID) (n: number of trajectories; mean value ± s.d.). **h**-**i**, **h**, Stably bound fractions and **i**, mean residence times of RNAPII before and after Mediator degradation (n = 10,000 resamplings; mean value ± s.d.; two-tailed unpaired t-test). **j**, Model of reduction of RNAPII residence time in CTD9 mutant.

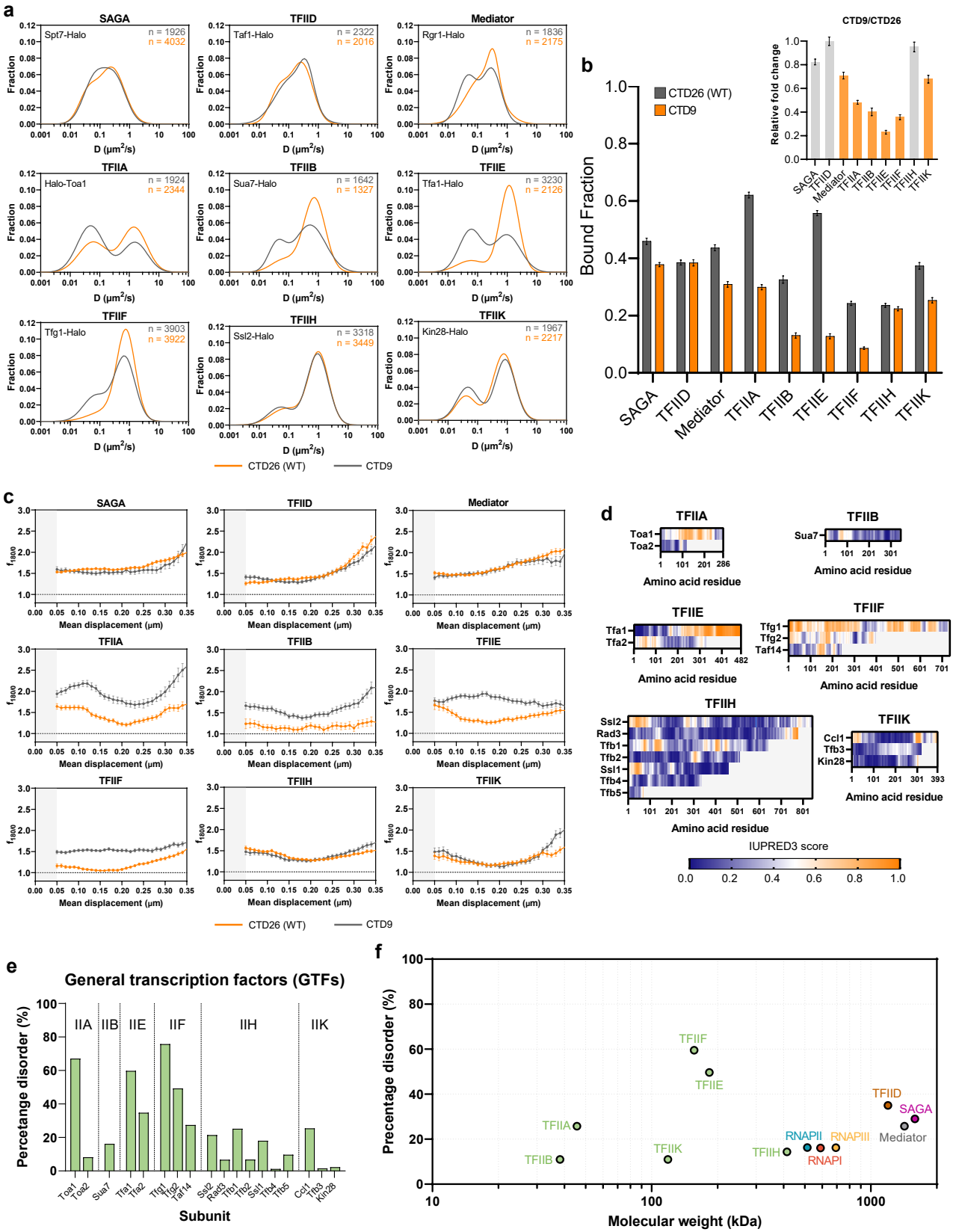

Fig. 6. CTD truncation impairs PIC formation and confinement of TFIIA, TFIIB, TFIIE, and TFIIF. a, Diffusion histogram for SAGA, TFIID, Mediator, TFIIA, TFIIB, TFIIE, TFIIF, TFIIH, and TFIIK in WT and CTD9 strains (n: number of trajectories). **b**, Fraction free and bound in WT and CTD9 strains. Relative fold change in the inner panel, with values lower than 0.8 highlighted in orange (n = 100 resamplings; mean value ± s.d.). **c**, $f_{180/0}$ plot in WT and CTD9 strains (n = 100 resamplings; mean value ± s.d.). **d**, IUPRED3 disorder scores for general transcription factors (GTFs). Residues with predicted scores above 0.5 considered disordered. **e**, Percentage disorder for individual subunits. **f**, Percentage disorder of selected transcription proteins.

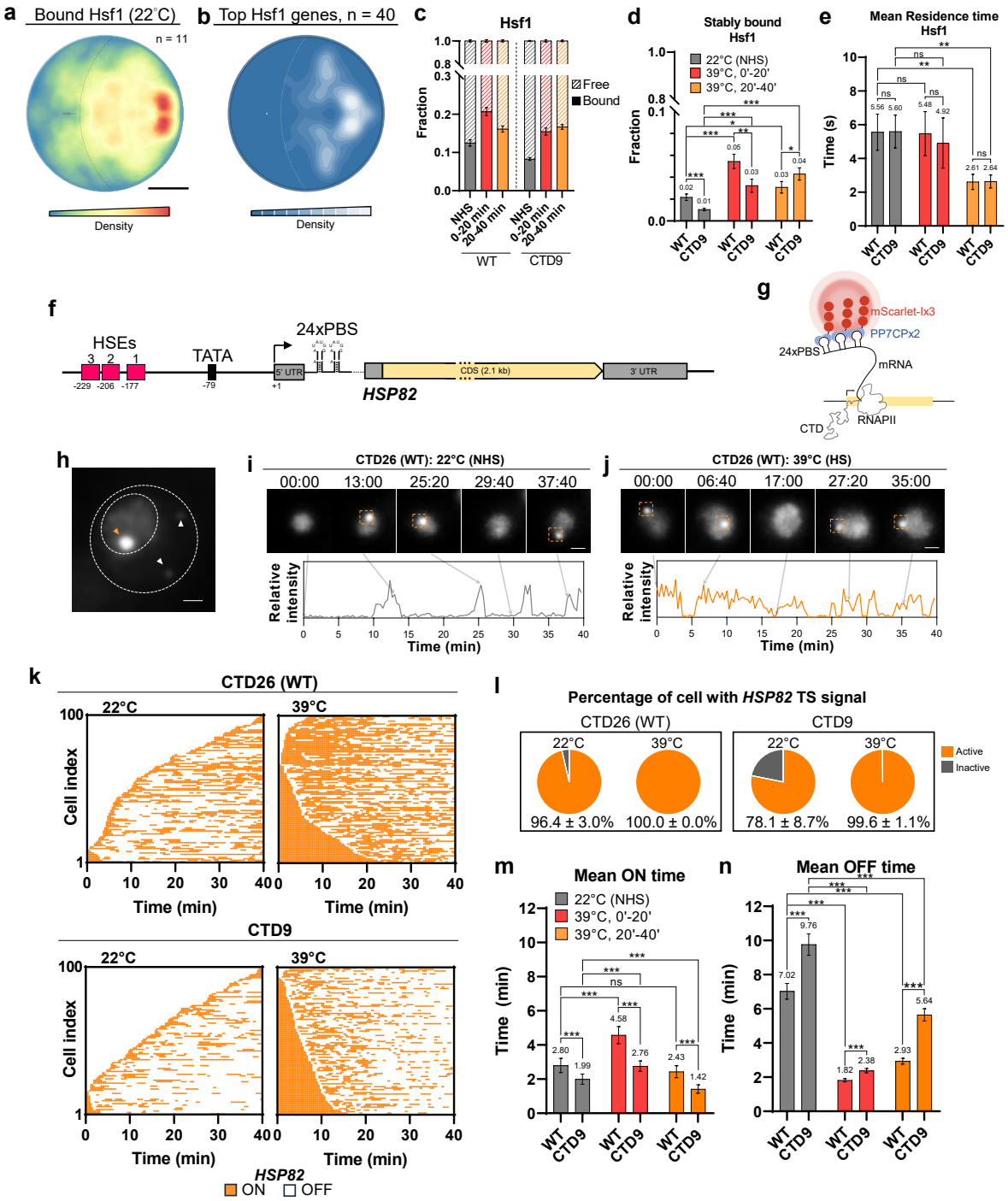

Fig. 7. CTD length controls burst size and frequency of *HSP82* gene transcription. **a**, Spatiotemporal map of bound Hsf1-Halo trajectories. Scale bar: 0.5 µm. **b**, Simulation of top Hsf1 target genes (HSF1Base[59]; n: number of genes). **c**-**e**, **c**, Fraction free and bound (n = 100 resamplings; mean value ± s.d.), **d**, stably bound fractions (n = 10,000 resamplings; mean value ± s.d.; two-tailed unpaired t-test) and **e**, mean residence times (n = 10,000 resamplings; mean value ± s.d.; two-tailed unpaired t-test) of Hsf1-Halo on heat shock (HS). CTD9 mutant shows similar upregulation of Hsf1 binding during acute heat shock (HS) compared to WT, but with slightly lower basal levels. Unlike WT, the CTD9 mutant maintains Hsf1 binding at the induced level during the prolonged response. The residence time of Hsf1 is comparable between WT and CTD9 under normal heat shock (NHS) and HS conditions. Overall, the dynamics of Hsf1 exhibit minimal change in CTD9 mutant. **f**, *HSP82* gene contains three characterized heat shock elements (HSEs) for Hsf1 binding[60]. 24x PP7 binding site (PBS) inserted within the 5' UTR of *HSP82* gene. **g**, Nascent *HSP82* mRNA visualized by PP7CPx2-mScarlet-Ix3 binding. **h**, Nascent mRNAs on *HSP82* transcription site (TS) as a bright spot in the nucleus (orange arrow). Cytoplasmic *HSP82* mRNAs indicated by white arrows. Scale bar: 1.0 µm. **i**-**j**, Maximum z-projected time-lapse images of PP7-*HSP82* cells. Scale bar: 1.0 µm (top). Trace of relative fluorescence intensity of the transcription site (bottom). k, Binarized rastergrams of the PP7 signal at the *HSP82* TS of 100 cells, ordered by time of first detection. **l**, % cells with *HSP82* TS signal. **m**-**n**, **m**, Mean ON time and **n**, mean OFF time of *HSP82* transcription (n = 10,000 resamplings; mean value ± s.d.; two-tailed unpaired t-test).

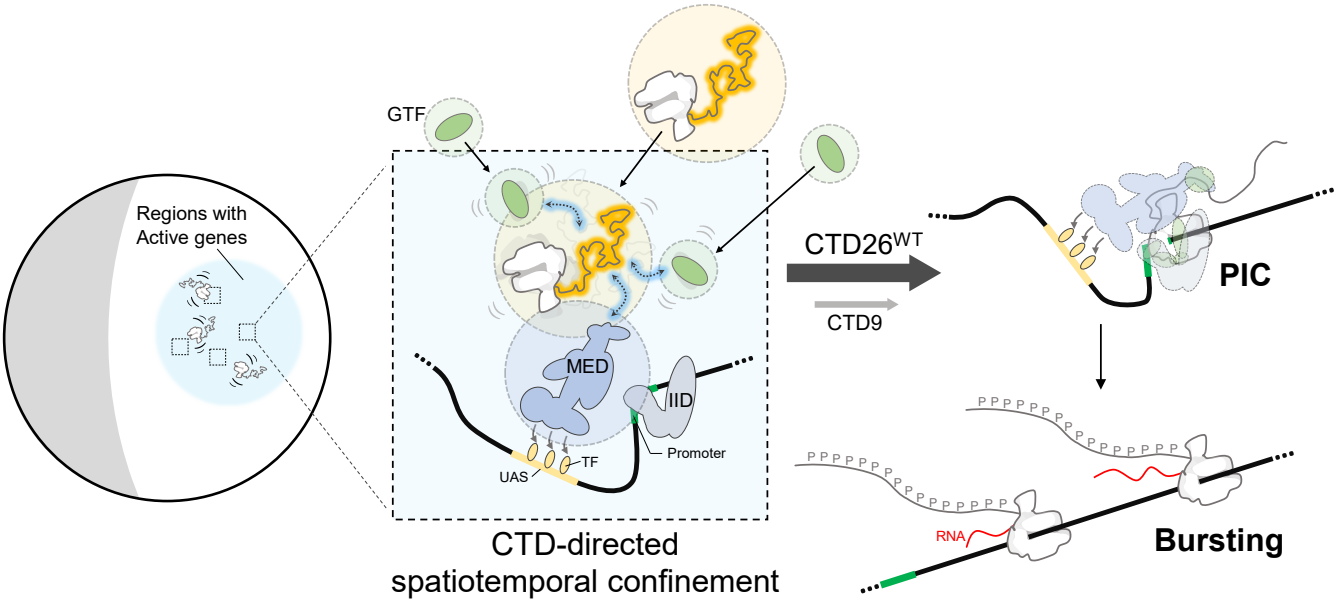

Fig. 8. CTD directs subnuclear confinement and chromatin binding of RNAPII for efficient PIC assembly and transcription bursting. In the yeast nucleus, telomere tethering of yeast chromosomes creates subnuclear regions enriched with active genes (left blue circle). Within these regions, the diffusion of RNAPII is confined by weak, long-range, transient CTD-Mediator interactions near an active promoter (middle square), leading to localized oversampling and enhanced target search. Subnuclear exploration of PIC components might also be confined by similar weak IDR-IDR interactions involving the CTD. Beyond spatial confinement, an increased hydrodynamic volume, attributed to IDRs, could amplify intermolecular interaction probabilities and specific association rates[61]. The combined effect of spatial confinement and elevated intermolecular interactions promotes the assembly kinetics of a complete PIC, thereby facilitating multiple rounds of RNAPII binding and activation during a transcription burst. GTF: General transcription factor; IID: TFIID; MED: Mediator; TF: Transcription factor; UAS: Upstream activating sequence.

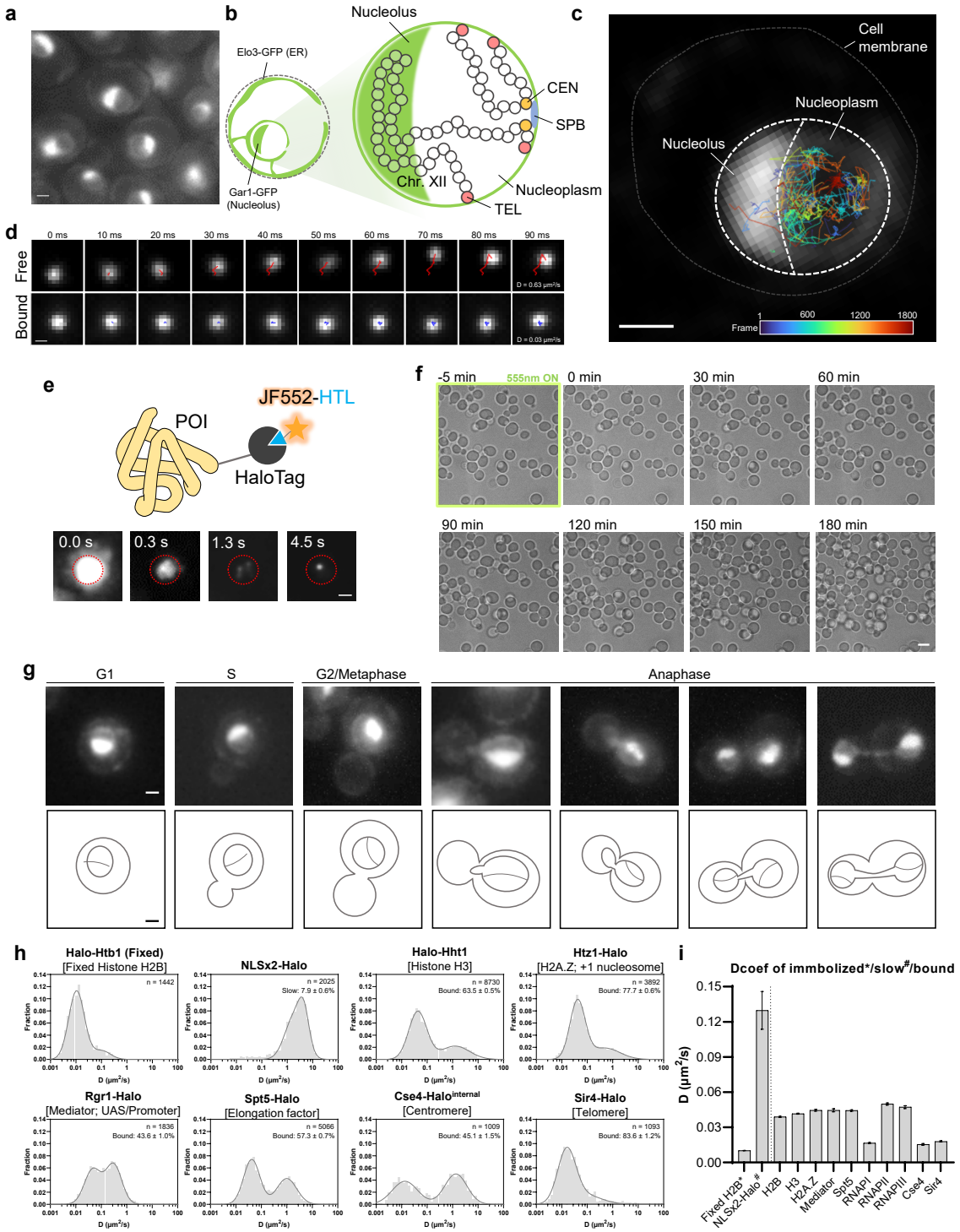

Extended Data Fig. 1 Single-molecule tracking in living yeast. **a**, ER and nucleolus shown by Elo3-GFP and Gar1-GFP. Scale bar: 1.0 µm. **b**, Coarse-grained representation of yeast interphase chromosomes, physically constrained by telomere (TEL)-nuclear envelope and centromere-spindle pole body (CEN-SPB) tethering. **c**, Overlay of RPB1^{Rpo21}-Halo^{JF552} trajectories on the nucleus relative to ER and nucleolar GFP markers. Rainbow colors indicate the first appearance of each trajectory. Scale bar: 1 µm. **d**, Single-molecule trajectories of RPB1^{Rpo21}-Halo^{JF552} (free or bound) with diffusion coefficients. Scale bar: 0.2 µm. **e**, Protein of interested (POI) fused with HaloTag, labeled with JF552-HaloTag ligand (JF552-HTL) (Top). Initial laser exposure of JF552 resulted in strong 'nuclear glow', followed by shelving in dark state and stochastic reactivation, leading to single-molecule detection. Nucleus circled in red. Scale bar: 1.0 µm. (Bottom). **f**, Strong 555 nm laser exposure for 5 min does not result in noticeable cell death or growth arrest. **g**, ER and nucleolar GFP markers for cell cycle stage identification. Scale bar: 1.0 µm. **h**, Diffusion coefficient histograms of various nuclear proteins (n: number of trajectories; mean value ± s.d.). **i**, Assessing diffusion coefficients of the immobilized/slow/bound population reveals no significant difference between histones and proteins that can move along DNA (e.g. RNAPII, RNAPIII, Spt5), while nucleolar RNAPI, and proteins that are physically tethered (Cse4 and Sir4) have significantly lower values (n = 100 resamplings; mean value ± s.d.).

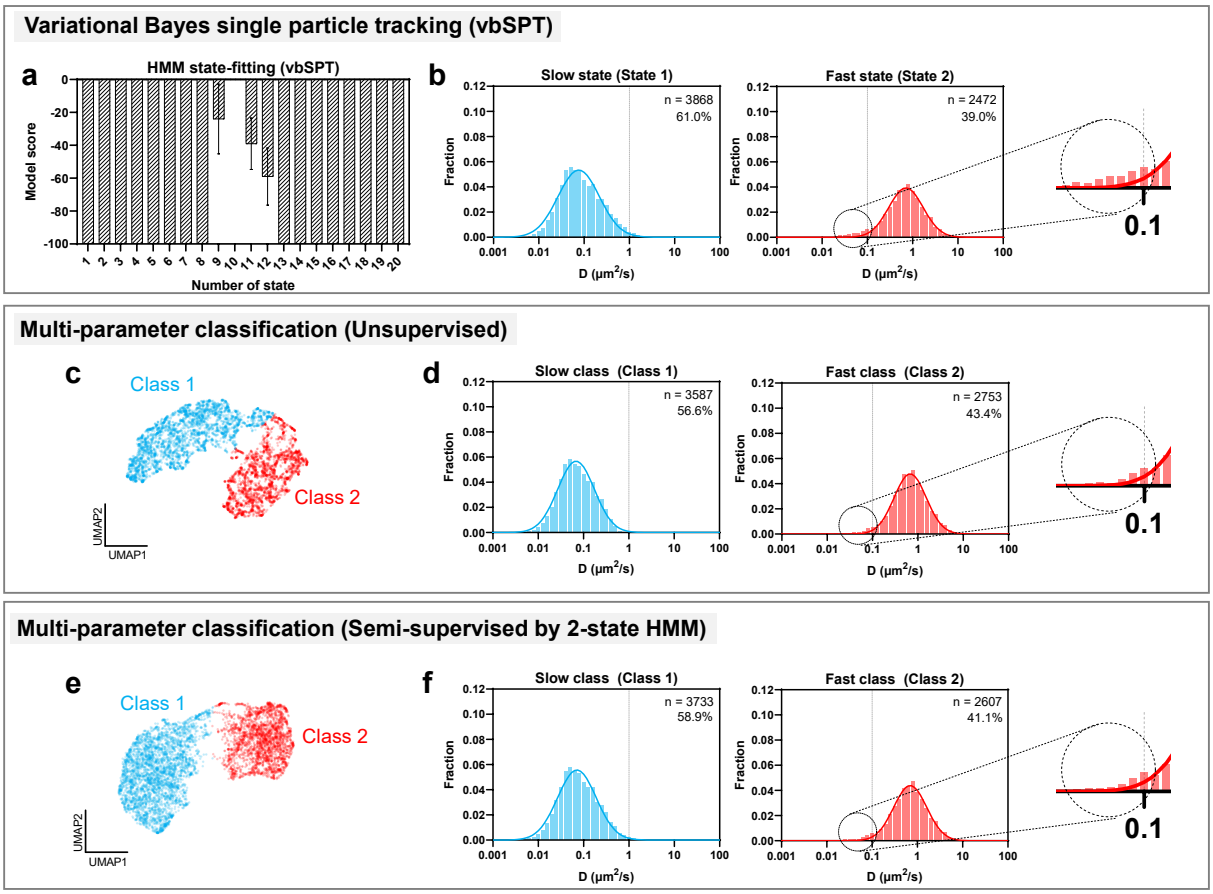

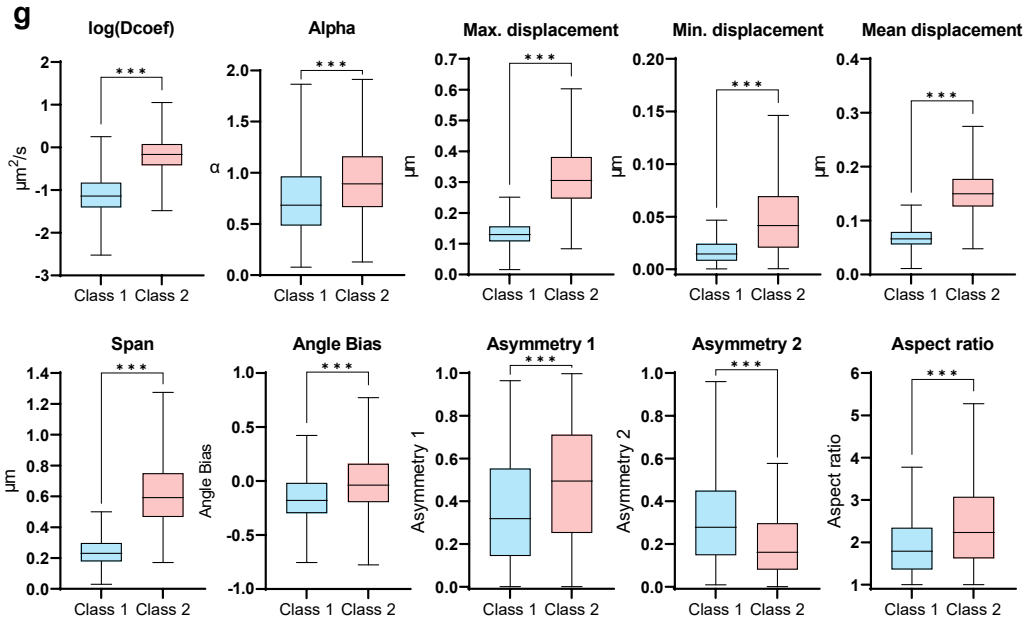

Extended Data Fig. 2 Multi-parameter classification of trajectories. a, Unsupervised vbSPT overfits SMT data of RNAPII (n = 100 resamplings; mean value ± s.d.). **b**, Diffusion coefficient histogram for fast and slow states from 2-state HMM using vbSPT. A minor fraction of very slowly diffusing trajectories was misclassified as fast-state (dashed circle) (n: number of trajectories; mean value ± s.d.). **c**, Unsupervised multi-parameter classification of RNAPII trajectories with UMAP dimension reduction and GMM clustering. **d**, Diffusion coefficient (D) distribution for the classified clusters (n: number of trajectories; mean value ± s.d.). **e**-**f**, similar to **c**-**d**, but with multi-parameter classification semi-supervised by 2-state HMM. **d** and **f**, Compared to **b**, Fast-class diffusion coefficient distribution showed less tailing (dashed circle). **g**, 10 parameters used for classification and their distributions in identified classes (refers **f** for n numbers; median (line), IQR (box), and min-max values (whiskers); two-tailed unpaired t-test).

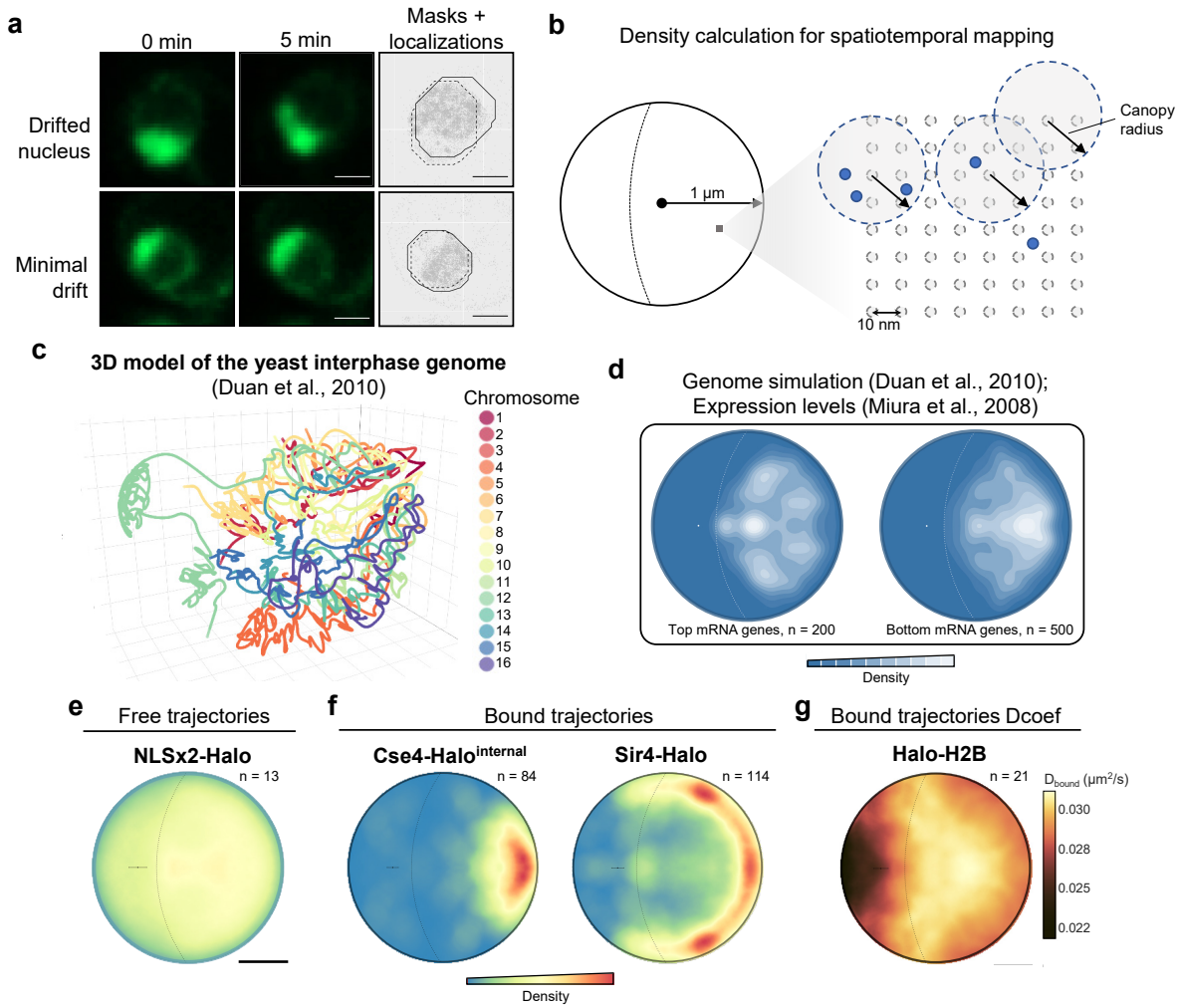

Extended Data Fig. 3 Spatiotemporal mapping reveals dynamics of nucleosome and nuclear landmark proteins. a, Nuclei in G1 cells with minimal drift selected for spatiotemporal mapping. Scale bar: 1.0 µm. **b**, Localization density calculated using 150 nm canopy radius from 10 nm bins. **c**, 3D simulation of the yeast interphase genome based on 3C data[22]. **d**, Top and bottom mRNA genes simulation maps based on gene expression data in minimal medium[49]. Left panel is reuse of Fig. 1d top panel (n: number of genes). **e**, Freely diffusing NLSx2-Halo map. Scale bar: 0.5 µm. **f**, Bound Cse4 (left) and Sir4 (right) maps (Error bar: centroid of nucleolus ± s.d.; n: number of nuclei). Sir4 bound map showed dense regions proximal and distal to the centromere, mirroring the telomere clusters of short and long chromosomes[20,22,62]. **g**, Bound H2B diffusion coefficient map. Scale bar: 0.5 µm (Error bar: centroid of nucleolus ± s.d.; n: number of nuclei). Telomere and centromere movements are confined due to attachment to the nuclear envelope and spindle pole body, respectively[63]. Likewise, the local diffusion coefficients of chromatin-bound H2B reveal lower histone dynamics near centromeres and telomeres (Extended Data Fig. 1h,i).

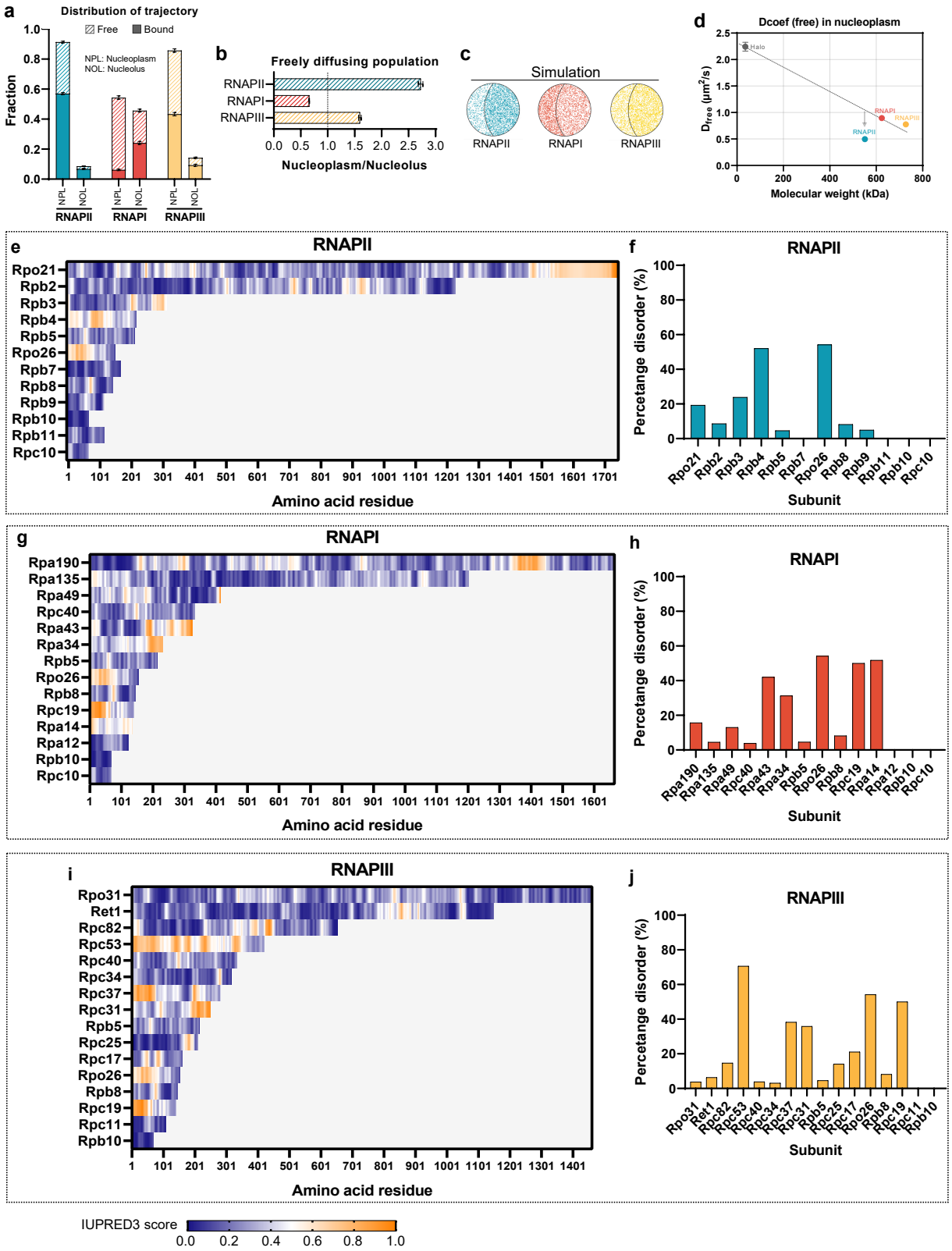

Extended Data Fig. 4 Spatiotemporal dynamics of RNAPII, RNAPI and RNAPIII. a, Fraction of free and bound in nucleoplasm (NPL) and nucleolus (NOL) (n = 100 resamplings; mean value ± s.d.). **b**, Distribution (area normalized) of free RNAPII, RNAPI and RNAPIII in nucleoplasm and nucleolus (n = 100 resamplings; mean value ± s.d.). **c**, Simulation of Nucleoplasm/Nucleolus distribution. **d**, Diffusion coefficients and molecular weights of free RNAPII, RNAPI and RNAPIII in nucleoplasm (n = 100 resamplings; mean value ± s.d.). **e**,**g**,**i**, IUPRED3 disorder scores for subunits of RNAPII, RNAPI and RNAPIII. Residues with predicted scores above 0.5 considered disordered. **f**,**h**,**j**, Percentage disorder for individual subunits.

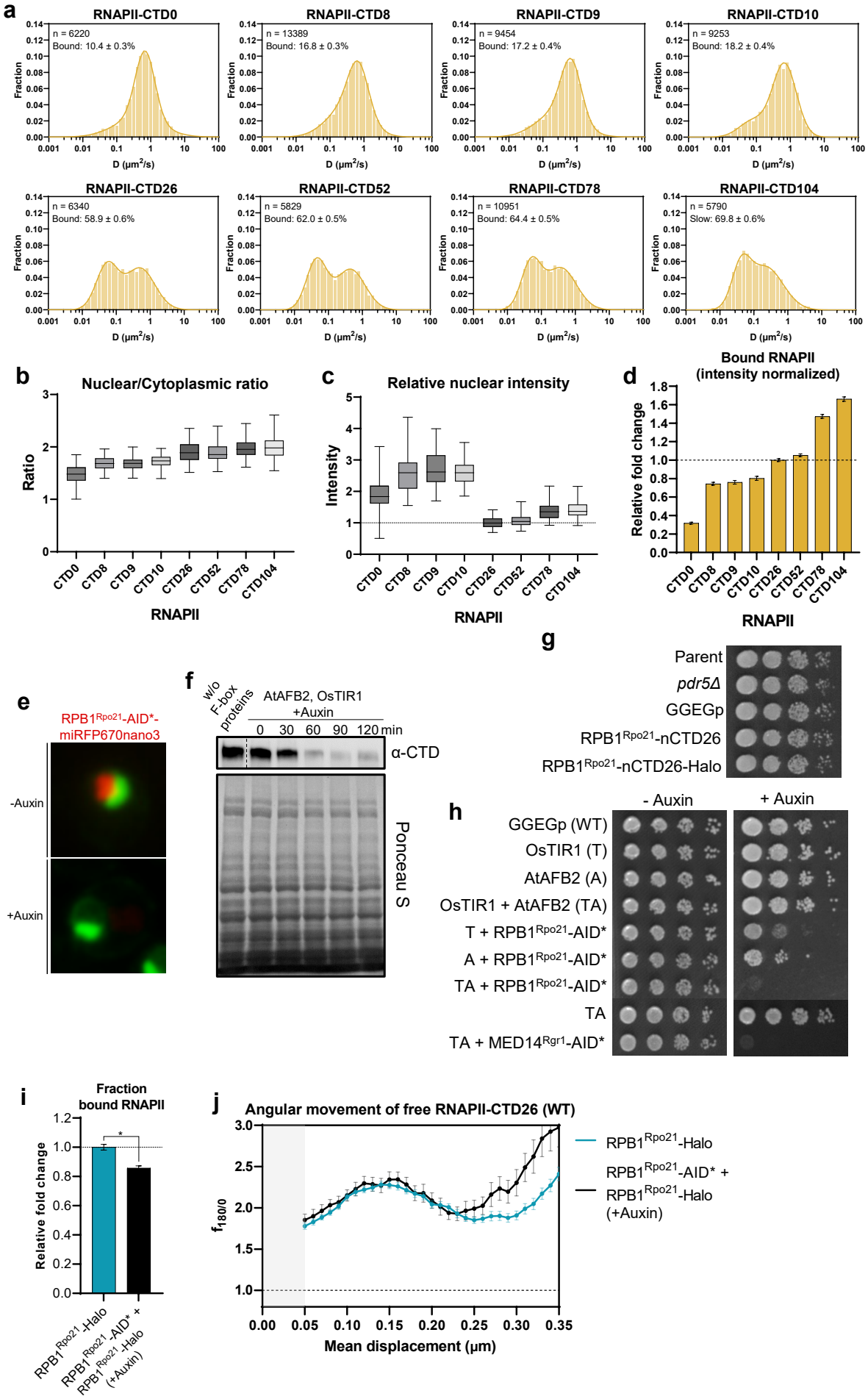
a
RNAPII-CTD0
n = 6220
Bound: 10.4 ± 0.3%
RNAPII-CTD8
n = 13389
Bound: 16.8 ± 0.3%
RNAPII-CTD9
n = 9454
Bound: 17.2 ± 0.4%
RNAPII-CTD10
n = 9253
Bound: 18.2 ± 0.4%
RNAPII-CTD26
n = 6340
Bound: 58.9 ± 0.6%
RNAPII-CTD52
n = 5829
Bound: 62.0 ± 0.5%
RNAPII-CTD78
n = 10951
Bound: 64.4 ± 0.5%
RNAPII-CTD104
n = 5790
Slow: 69.8 ± 0.6%
Fraction
D (μm²/s)
b
Nuclear/Cytoplasmic ratio
Ratio
c
Relative nuclear intensity
Intensity
d
Bound RNAPII
(intensity normalized)
Relative fold change
CTD0
CTD8
CTD9
CTD10
CTD26
CTD52
CTD78
CTD104
RNAPII
e
RPB1Rpo21-AID*-
miRFP670nano3
-Auxin
+Auxin
f
w/o
F-box
proteins
AtAFB2, OsTIR1
+Auxin
0 30 60 90 120 min
α-CTD
Ponceau S
g
Parent
pdr5Δ
GGEGp
RPB1Rpo21-nCTD26
RPB1Rpo21-nCTD26-Halo
h
- Auxin
+ Auxin
GGEGp (WT)
OsTIR1 (T)
AtAFB2 (A)
OsTIR1 + AtAFB2 (TA)
T + RPB1Rpo21-AID*
A + RPB1Rpo21-AID*
TA + RPB1Rpo21-AID*
TA
TA + MED14Rgr1-AID*
i
Fraction
bound RNAPII
Relative fold change
RPB1Rpo21-Halo
RPB1Rpo21-AID* +
RPB1Rpo21-Halo
(+Auxin)
j
Angular movement of free RNAPII-CTD26 (WT)
f180/0
Mean displacement (μm)
RPB1Rpo21-Halo
RPB1Rpo21-AID* +
RPB1Rpo21-Halo
(+Auxin)

Extended Data Fig. 5 CTD length affects RNAPII subcellular distribution and expression. **a**, Diffusion coefficient histogram for RNAPII with varying CTD lengths (n: number of trajectories; mean value ± s.d.). **b**-**c**, **b**, nuclear/cytoplasmic ratio and **c**, relative nuclear intensity of WT RNAPII and CTD mutants (n $\geq$ 50 nuclei; median (line), IQR (box), and min-max values (whiskers)). Consistent with previous study, we observed an overexpression of RNAPII for CTD truncation mutants[8], and additionally detected an increased RPB1^{Rpo21} signal in the cytoplasm and nucleolus. **d**, Amount of bound RNAPII normalized to nuclear intensity (n = 100 resamplings; mean value ± s.d.). **e**, Fluorescence signal of RPB1^{Rpo21}-AID*-miRFP670nano3 (red) before and after RNAPII degradation by auxin. Nucleolar and ER markers in green. Scale bar: 1.0 µm. **f**, Western blot showing time course degradation of RPB1^{Rpo21}-AID* by auxin, detected using CTD antibody (top), and Ponceau S staining on total protein (bottom). **g**, Spot assay for strains with *pdr5*Δ, GFP markers (GGEGp), RPB1^{Rpo21}-nCDT26, or RPB1^{Rpo21}-nCDT26-Halo showing identical growth. **h**, Spot assay demonstrating impaired cell growth for RPB1^{Rpo21} or MED14^{Rgr1} AID degron. All AID* constructs contain miRFP670nano3 as a fluorescence marker. **i**-**j**, Cells expressing ectopic RPB1^{Rpo21}-Halo in an RPB1^{Rpo21} AID background show minimal changes in the **i**, bound fraction and **j**, $f_{180/0}$ of RNAPII after auxin treatment, compared to those in WT expressing RPB1^{Rpo21}-Halo.

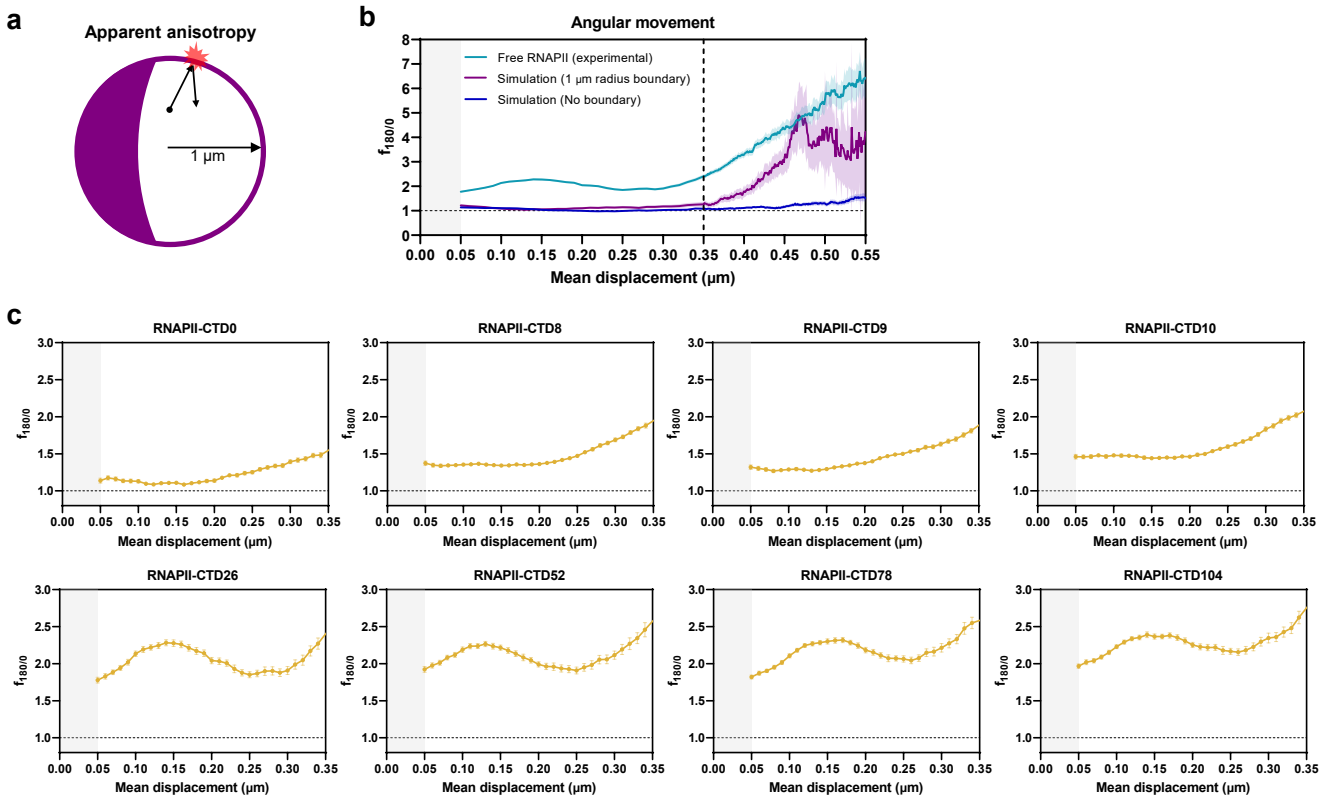

Extended Data Fig. 6 CTD length impacts free RNAPII anisotropy. a, Apparent anisotropy due to nuclear confinement in small yeast nucleus. **b**, Brownian simulations indicate significant apparent anisotropy for mean displacement longer than 350 nm (n = 100 resamplings; mean value ± s.d.). **c**, CTD length increase leads to an elevation in $f_{180/0}$ trend (n = 100 resamplings; mean value ± s.d.).

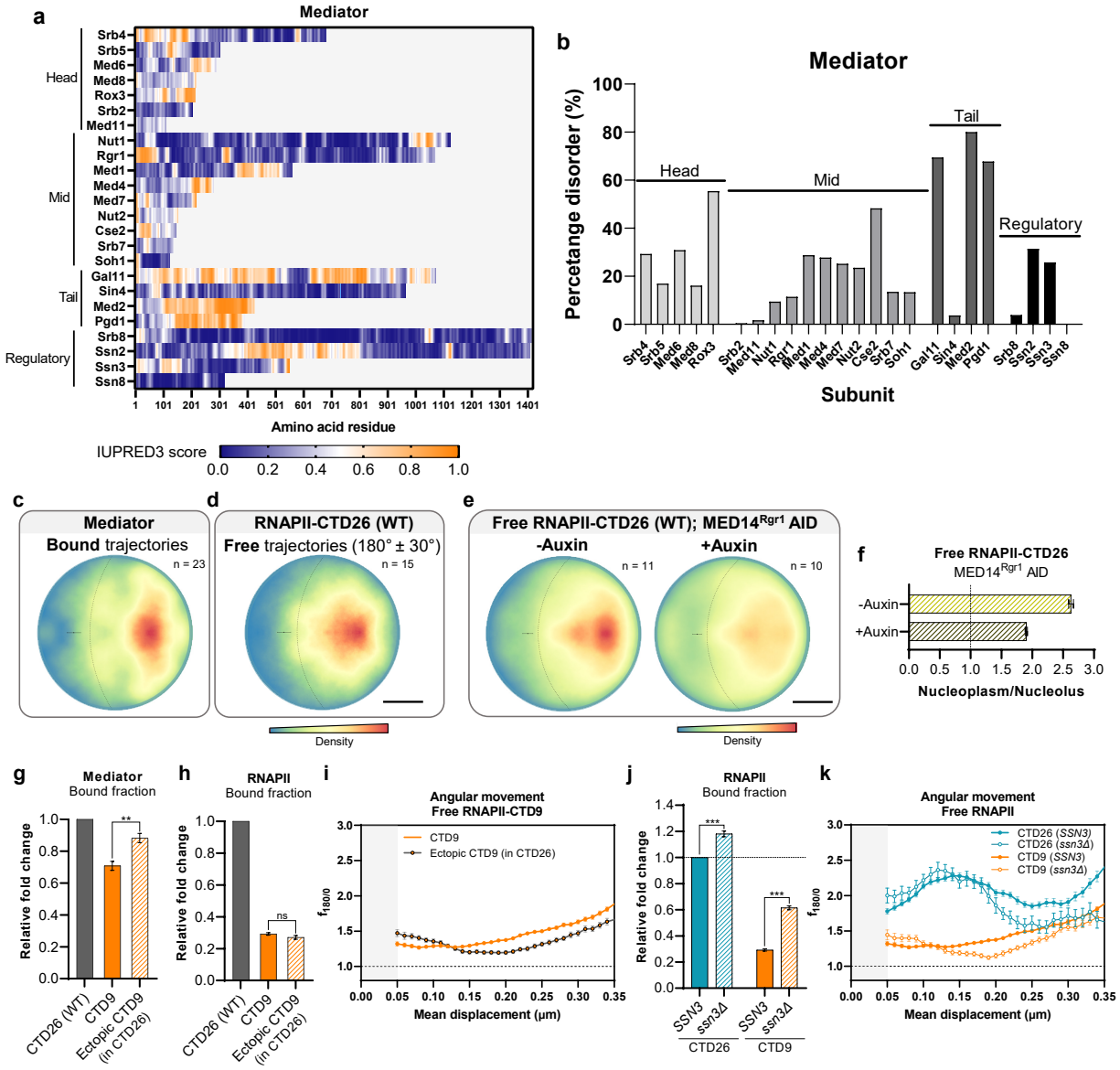

Extended Data Fig. 7 Investigating the role of Mediator in spatiotemporal confinement of RNAPII a, IUPRED3 disorder scores for Mediator subunits. Residues with predicted scores above 0.5 considered disordered. **b**, Percentage disorder for individual subunits. **c**, Bound Mediator map. **d**, Free RNAPII-CTD26 map showing confined trajectories. Scale bar: 0.5 μm. (Error bar: centroid of nucleolus ± s.d.; n: number of nuclei). **e**, Free RNAPII-CTD26 map in MED14^{Rgr1} AID background before and after auxin treatment. Scale bar: 0.5 μm (Error bar: centroid of nucleolus ± s.d.; n: number of nuclei). **f**, Nucleoplasm/Nucleolus value of RNPAII-CTD26 in MED14^{Rgr1} AID background before and after auxin treatment (n = 100 resamplings; mean value ± s.d.). Although increased hydrodynamic volume conferred by the disordered CTD (Fig. 2c and Extended Data Fig. 10c) could contribute to size exclusion of RNAPII from the nucleolus, resulting in nucleoplasmic concentration and confinement, it is notable that degradation of Mediator (MED14^{Rgr1} AID) allows diffusion of full-length RNAPII into the nucleolus, indicating the importance of active restraint by the Mediator. **g**-**i**, **g**, Relative Mediator bound fraction, **h**, relative RNAPII bound fraction and **i**, $f_{180/0}$ for RNAPII-CTD9 as sole source, or ectopically expressed in CTD26 (WT) background (n = 100 resamplings; mean value ± s.d.; two-tailed unpaired t-test). The reduction of Mediator binding in the CTD9 mutant (Fig. 6a,b) led us to examine if this contributed to the observed RNAPII-CTD9 dynamics (Fig. 2 and 3). We find that despite restored Mediator binding in a strain co-expressing RPB1^{Rpo21}-CTD26 (WT) and RPB1^{Rpo21}-CTD9, RNAPII-CTD9 still showed a significant decrease in bound fraction and near-isotropic diffusion, suggesting that the altered RNAPII dynamics is a directed consequence of CTD truncation, instead of a reduction in Mediator binding. **j**, Relative fraction bound of RNAPII-CTD26 and RNAPII-CTD9 in WT and *ssn3*Δ (n = 100 resamplings; mean value ± s.d.; two-tailed unpaired t-test). **k**, $f_{180/0}$ plot for RNAPII-CTD26 and RNAPII-CTD9 in WT and *ssn3*Δ (n = 100 resamplings; mean value ± s.d.). **j**-**k**, During PIC formation, interaction between the Mediator and RNAPII can be obstructed by the Mediator regulatory subcomplex, the 4-subunit Cdk8 kinase module (CKM)[64-66]. Deficiency of Cdk8^{SSN3} (*ssn3*Δ) promotes stable Mediator-RNAPII interactions[64]. Importantly, increasing the frequency of stable interactions between Mediator and RNAPII does not affect the confinement of free RNAPII, as little or no change in the anisotropy ($f_{180/0}$) of free RNAPII is observed in the *ssn3*Δ mutant.

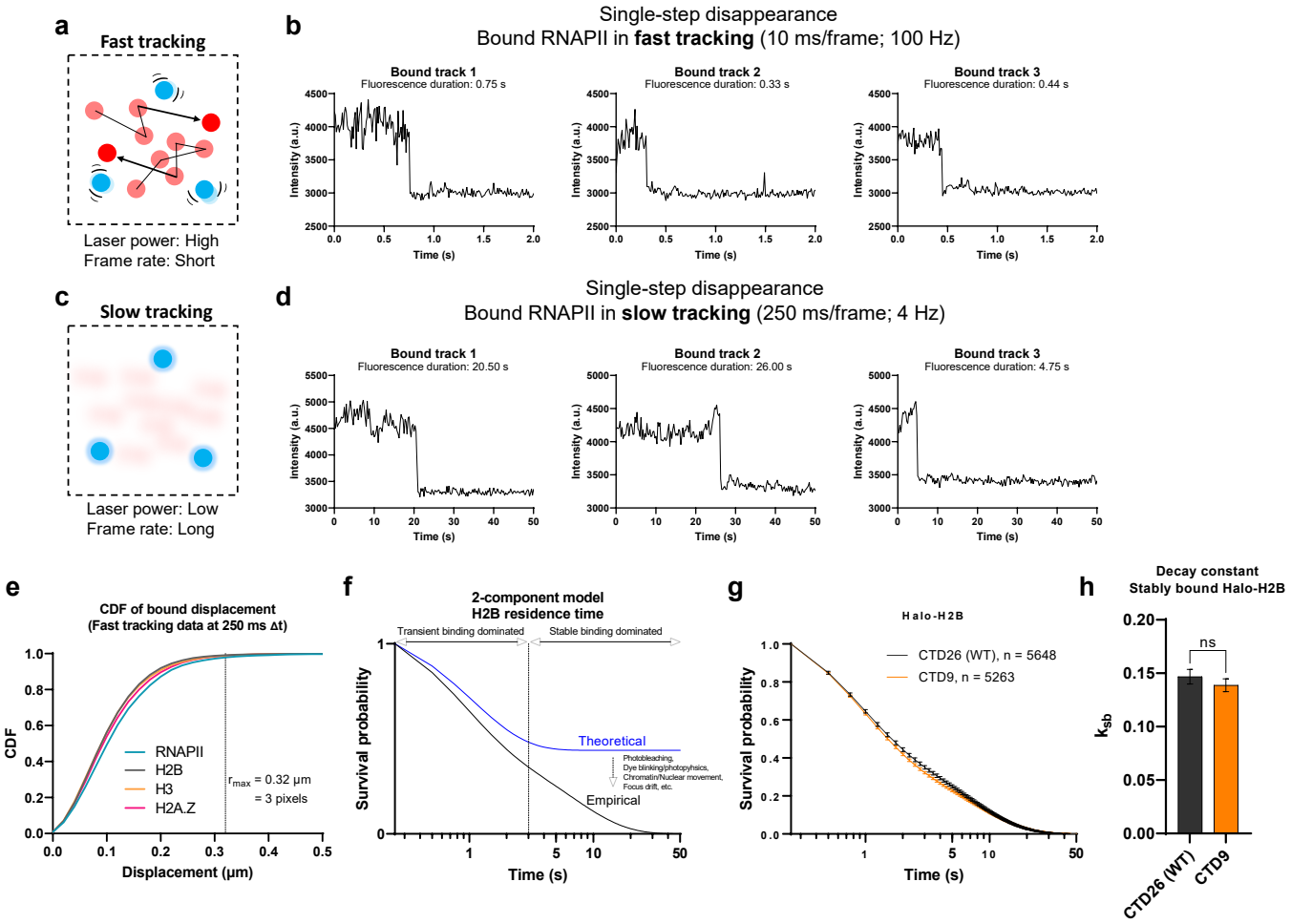

Extended Data Fig. 8 Fast and slow tracking mode of single-molecule tracking. **a**, Fast tracking with high laser power and short frame rate (10 ms/frame) reveals diffusive dynamics of free (red) and bound (blue) molecules. **b**, Single-step disappearance of chromatin-bound RNAPII in fast tracking. **c**, Slow tracking with low laser power and long frame rate (250 ms/frame) reveals residence time of bound molecules (blue). **d**, Single-step disappearance of chromatin-bound RNAPII in slow tracking. **b**-**d**, Here we term 'disappearance' as we cannot definitively differentiate between the molecule diffusing out of the focal plane or photobleaching within the living cell. **e**, CDF of bound displacement of RNAPII, H2B, H3 and H2A.Z to determine the r_{max} for trajectory linking in slow tracking[67]. **f**, In G1 cells, nucleosomal H2B (representing the stable binding population) was hypothesized to bind for a sufficiently long period, such that during image acquisition, their dissociation was barely observed. Nonetheless, the observed residence times for H2B typically fall within 30 seconds, due to factors such as photobleaching, dye blinking, chromatin/nuclear movements, and focus drift. **g**, Survival probability of Halo-H2B observed residence times in CTD26 (WT) and CTD9 strains (n: number of trajectories; mean value ± s.d.). **h**, Decay constant of stably bound Halo-H2B (k_{sb}) in CTD26 (WT) and CTD9 strains (mean value ± s.d.).

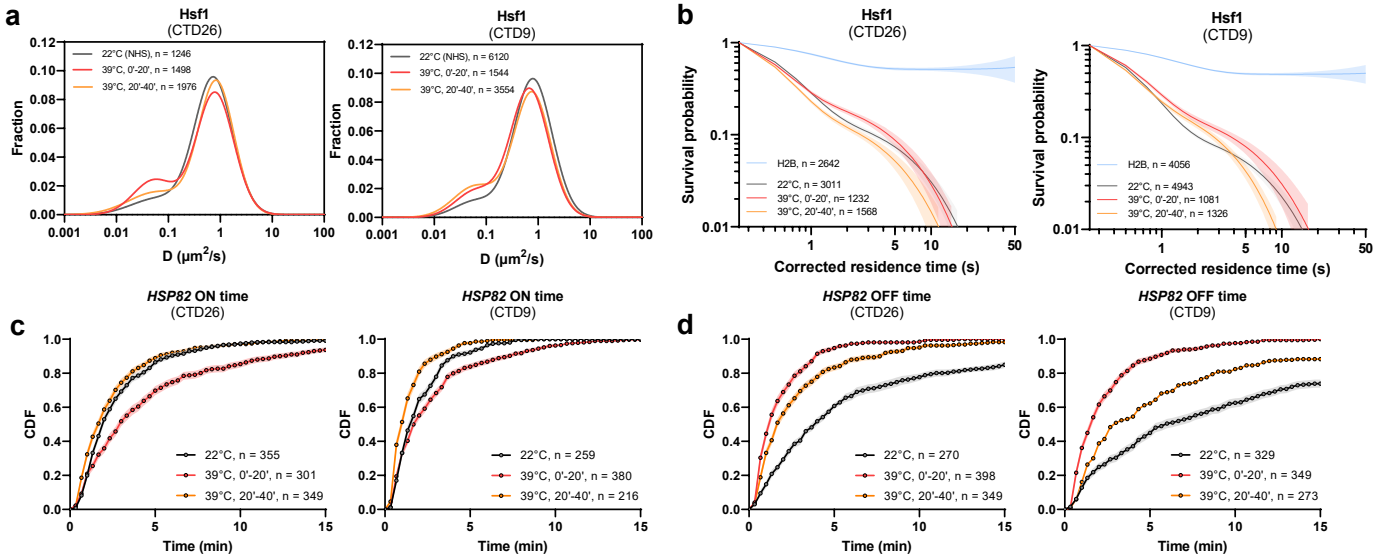

Extended Data Fig.9 CTD length controls *HSP82* transcription bursting, with minimal effect on Hsf1 dynamics. a-b, **a**, Diffusion coefficient histograms for Hsf1-Halo and **b**, survival probability of bound Hsf1-Halo under heat shock in CTD26 (WT) (left) and CTD9 (right) strains (n: number of trajectories; mean value ± s.d.). **c-d**, **c**, *HSP82* ON time and **d**, OFF time cumulative distribution function (CDF) under heat shock in CTD26 (WT) (left) and CTD9 (right) strains (n: number of ON or OFF events; mean value ± s.d.).

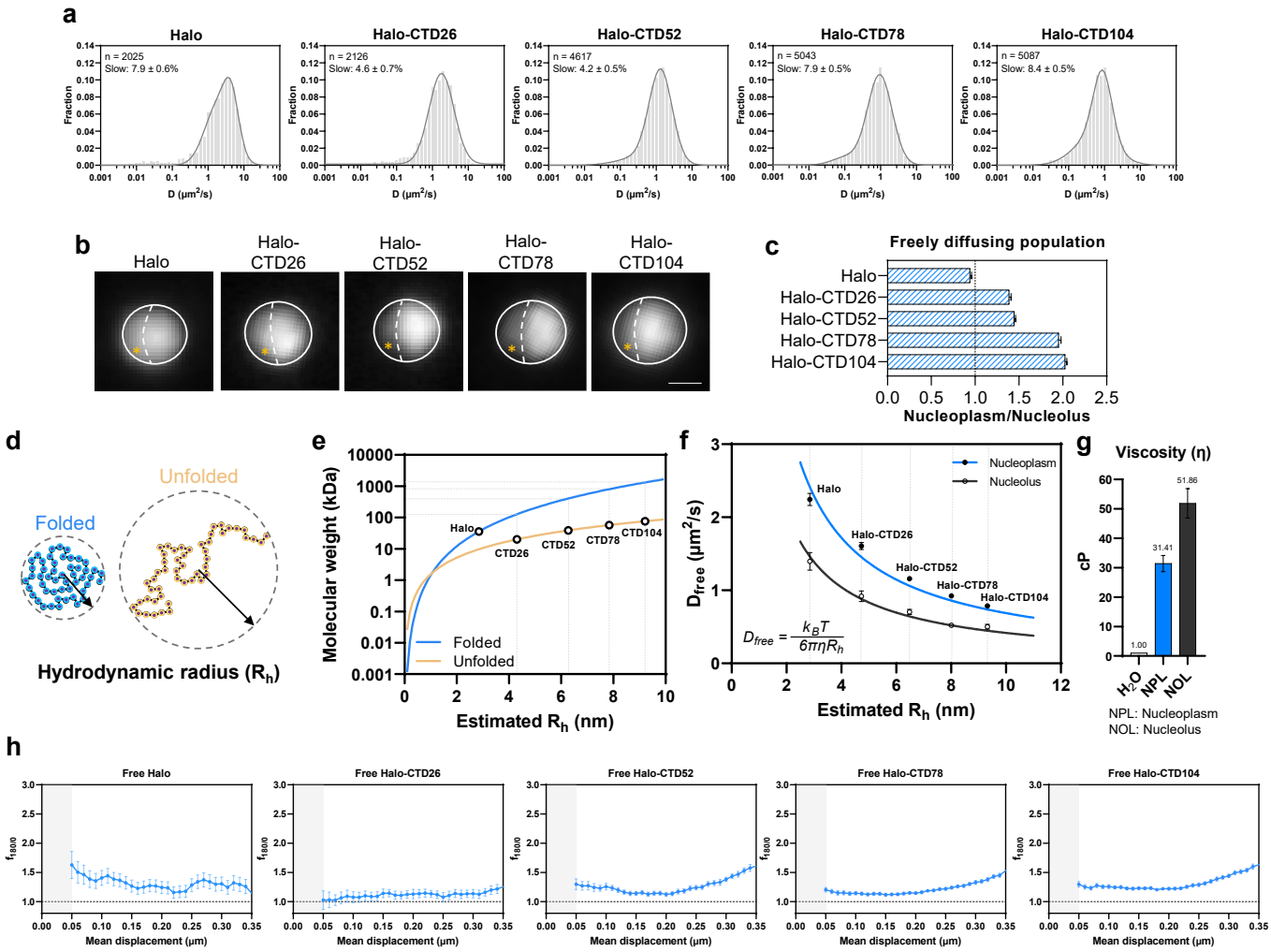

Extended Data Fig. 10 CTD is necessary but not sufficient for confining protein diffusion. **a**, HaloTag (NLSx2-Halo) and Halo-CTD fusions diffusion coefficient histogram by CTD length (n: number of trajectories; mean value ± s.d.). The first plot is reuse of the top panel's second plot from Extended Data Fig. 1h. **b**, HaloTag and Halo-CTD fusions bulk wide-field staining using JFX650 in live cell. Scale bar: 1.0 μm. **c**, Nucleoplasm/Nucleolus ratios for freely diffusing HaloTag and Halo-CTD fusions (n = 100 resamplings; mean value ± s.d.). **d**, Protein disorder affects hydrodynamic radius (R_h). **e**, Theoretical relationship between molecule weight and R_h for folded and unfolded peptides (Data from Fluidic Analytics). **f**-**g**, **f**, D_{free} and estimated R_h of the HaloTag and Halo-CTD fusions in nucleoplasm and nucleolus. Data fitted with Stokes-Einstein equation to calculate **g**, apparent viscosity (η) of yeast nucleoplasm and nucleolus, respectively. K_B: Boltzmann's constant. T: Temperature in Kelvin; 295.15K (22°C) (n = 100 resamplings; mean value ± s.d.). **h**, $f_{180/0}$ plot for HaloTag and Halo-CTD fusions (n = 100 resamplings; mean value ± s.d.).